https://doi.org/10.1016/j.engfracmech.2023.109284

Analytical model for near-crack debonding in fiber-reinforced polymer composite-overlaid metallic plates with a central crack

Bo-Tong Zheng[a,b] and Jin-Guang Teng[a]*

[a]Department of Civil and Environmental Engineering, The Hong Kong Polytechnic University, Hong Kong, China.

[b]Sonny Astani Department of Civil and Environmental Engineering, University of Southern California, United States.

*Corresponding author, E-mail: cejgteng@polyu.edu.hk

E-mail: botongzh@usc.edu (Bo-Tong Zheng)

Abstract

Extensive research has been undertaken on the use of fiber-reinforced polymer (FRP) in the strengthening of fatigue-damaged and fatigue-prone civil engineering metallic structures. Evaluation of the static load-bearing capacity and fatigue life of the so-strengthened structures necessitates the accurate prediction of the stress intensity factor (SIF) for an FRP-overlaid crack in a metallic structure. This paper first presents a new analytical model for predicting the near-crack interfacial debonding process and its effect on the SIF of a centrally cracked metallic plate that is bonded on both sides with an FRP overlay. The stress distributions in both the overlays and the metallic plate, the interfacial shear stress distribution, the crack opening displacement profile, and the SIF can all be found without the need for any *a priori* assumption of the near-crack interfacial debonding process/pattern. The accuracy of the analytical model is evaluated with both finite element predictions and experimental data. The analytical model is then used to advance our understanding of the mechanisms of near-crack interfacial debonding, including both the initiation and propagation of debonding, as well as the effect of near-crack debonding on the SIF. It should

be noted that while the study was conducted with explicit reference to metallic plates bonded with FRP overlays, the analytical model is applicable to combinations of other materials as long as the substrate plate material is isotropic, and both components remain linear-elastic during the loading process.

Keywords: Fatigue crack; Stress intensity factor; Interfacial debonding; FRP; Strengthening.

1. Introduction

Metallic structures subjected to cyclic fatigue loadings such as aircraft, offshore oil platforms and wind turbines, subsea risers, hydro turbines, bridges, and highway structures are prone to cracking in regions with stress concentration. Fatigue cracks, if left unchecked, may cause catastrophic failures such as, among many others, the collapse of the Norwegian Alexander L. Kielland oil platform in 1981 in the North Sea (France, 2019), the collapse of the Mianus River bridge in 1983 in the US (Fisher et al., 1998), and the collapse of the Morandi Bridge (officially Viadotto Polcevera) in 2018 in Italy (Invernizzi et al., 2022), all resulting in casualties, negative social impacts, and considerable economic losses. Consequently, fatigue-damaged metallic structural components need to be either replaced or repaired to prevent the fracture of the component and failure of the overall structure. However, complete replacement of cracked components is often costly (Domazet, 1996) and sometimes infeasible (Shin et al., 1996). Therefore, rapid, non-interruptive, and cost-effective repairing methods are generally needed as remedies for fatigue-cracked metallic structures.

The mechanical behavior of a crack in a metallic structure depends on the stress distribution in the crack-tip vicinity (Figure 1a), which can be described by the stress intensity factor (SIF) (Irwin, 1957) in the context of linear elastic fracture mechanics (LEFM). If the SIF reaches the limit value of the material, referred to as the fracture toughness, the crack will undergo an unstable fast

extension leading to immediate fracture (Fisher et al., 1998). Generally, for a finite-dimension metallic member containing a crack, the SIF is linearly and nearly exponentially proportional to the applied load and the crack length, respectively (Figure 1b). Therefore, the longer the crack length is, the smaller is the load at which the crack fractures (i.e., load-bearing capacity). Under static loading, if the SIF is below the fracture toughness, the crack length remains unchanged. However, under fatigue loading (Figure 1c), the crack length will gradually grow with each load cycle. As the crack length increases, the SIF also increases, and the crack will fracture when the SIF reaches the fracture toughness at the maximum crack length attainable. The number of load cycles required for the crack to reach the maximum crack length is referred to as the *fatigue life*. The crack-growth rate, defined as the crack length extension per load cycle, appears to follow approximately a linear relationship with the SIF in the log-log domain (Paris and Erdogan, 1963; Elber, 1971) if the SIF range is above the fatigue threshold (Figure 1d). Therefore, the behavior of a crack under both static and fatigue loading conditions is determined by the SIF, the accurate prediction of which is critical to the evaluation of the load-bearing capacity and the fatigue life of cracked metallic structures.

All the repairing methods for fatigue-cracked metallic structures essentially aim at reducing the SIF. Conventional crack-repairing methods, such as the crack stop-hole method that involves the drilling of a hole at the crack-tip location (Razavi et al., 2017), crack welding (Jiao et al., 2012), and crack grinding (Rodríguez-Sánchez et al., 2011) practically eliminate the crack tip that causes the stress singularity there. These methods are widely used in field applications mainly due to their ease of operation. However, they damage the parent structure and introduce new stress concentrations at the periphery of the stop-hole, the weld toes, or the ground surfaces, where new cracks are likely to initiate and grow. Therefore, they are generally ineffective in recovering the

load-bearing capacity and arresting the fatigue crack growth, and they are inapplicable in many scenarios where damaging the parent structures is prohibited. A relatively more effective method is to attach overlaying reinforcement to a crack, which forms a parallel system and shares the load with the metallic substrate plate, hence reducing the load applied to the crack.

The use of metallic overlay plates to reinforce a cracked metallic structure usually involves the bolting or welding of bulky metallic plates as external reinforcement to the target structure. The methods is thus labor-intensive and induces new stress concentrations (Domazet, 1996). By contrast, fiber-reinforced polymer (FRP) composites have high stiffness/strength-to-weight ratios, and the external bonding of FRP reinforcement using adhesive does not damage the parent structure except to the extent of surface preparation. As a result, using FRP overlays to repair fatigue-cracked metallic structures has attracted increasing research attention in the past two decades as a rapid, non-interruptive, and effective measure to enhance the load-bearing capacity and extend the fatigue life of cracked metallic structures. The effectiveness has been experimentally demonstrated on cracked steel plates (Jones and Civjan, 2003; Colombi et al., 2015; Hu et al., 2016; Aljabar et al., 2017), flexural members with various cross-sections (Ghafoori et al., 2012a; Hmidan et al., 2014; Colombi and Fava, 2016; Yu and Wu, 2017)(Deng et al., 2023; Jiang et al., 2022), and large-scale girders (Tavakkolizadeh and Saadatmanesh, 2003; Wu et al., 2012; Yue et al., 2016). A comprehensive review on the strengthening of steel structures with FRP composites, including the enhancement of fatigue resistance with FRP, can be found in Teng et al. (2012).

For cracks repaired with mechanically attached, unbonded FRP overlays, the SIF can be directly obtained based on the load shared by the cracked substrate plate, which can be readily determined from the overlay-to-substrate stiffness ratio and the total applied load (i.e., the stiffness ratio

method). However, for a bonded FRP-repaired crack, the SIF could be much smaller than that for an unbonded FRP-repaired crack because the interfacial bond around the crack offers an additional resistance to the opening-up of the crack. This has been clearly demonstrated through the fatigue tests of cracked steel beams conducted by Ghafoori et al. (2012a), wherein the cracked beams were each repaired with either a bonded or unbonded FRP overlay. By examining the strain distribution along the FRP overlay, it was found that the bonded FRP overlay experienced strain concentration in a small region near the crack (i.e., the near-crack region), while the unbonded FRP overlay exhibited an even strain distribution. As a result, the fatigue life of the bonded FRP-repaired beam was about 66 times that of the unbonded FRP-repaired beam (Ghafoori et al., 2012a). Similar results indicating that the fatigue life of bonded FRP-repaired aluminum alloy plates was around 50% longer than that of unbonded FRP-repaired ones were reported by Mall and Conley (2009). Due to the near-crack strain/stress concentration, a local interfacial debonding process in the near-crack region has been observed in FRP-repaired cracked metallic members (Colombi et al., 2003; Sabelkin et al., 2006; Huawen et al., 2010; Zheng and Dawood, 2016), which further complicates the problem. The local debonding zone enlarges under fatigue loading while remaining local to the near-crack region, as observed in some studies (Mall and Conley, 2009; Hu et al., 2021). In other studies, complete debonding of an FRP overlay was observed (Tsouvalis et al., 2009), which is, however, believed to be due to debonding initiating from the end(s) of the overlay (i.e., near-end debonding). The present paper is focused on the impact of near-crack debonding and the SIF of a cracked metallic plate bonded with FRP overlays instead of the effect of near-end deboning, which is a separate issue and may be addressed by appropriate end anchorage measures. Indeed, the prediction of the SIF for a bonded FRP-overlaid crack depends on a thorough understanding of the intricate interaction between the cracked substrate plate and the bonded FRP overlays through the

interface that is likely to experience interfacial debonding near the crack. To this end, the following questions call for answers:

Q1. What is the mechanism of local interfacial debonding initiation near a crack? Although near-crack debonding has been numerically and experimentally observed, the fundamental cause of it, e.g., stress concentration or excessive slips, has not been properly explained.

Q2. Once a local interfacial debonding zone appears, what are the shape and size of it? It has been predominantly assumed that a near-crack debonding zone has an elliptical shape. However, this "consensus" lacks evidence and/or rigorous proof.

Q3. How to predict the propagation of local interfacial debonding? It has been unclear how the propagation of the crack influences the size and shape of the interfacial debonding zone, except for the widely adopted assumption that the debonding zone is elliptical and has the same longer dimension as the crack.

Q4. How to predict the SIF in the presence of local interfacial debonding? Accurate prediction of the SIF is the most important aspect for fatigue crack analysis. However, the interaction between interfacial debonding and the SIF has remained an unresolved issue.

Q5. Will interfacial debonding near a crack always remain local, or will it induce complete debonding? The relationship between near-crack debonding and complete debonding of the overlays from the substrate has always been only vaguely stated in existing studies, lacking a clear analytical examination.

It is evident that these questions are deeply entangled and must be answered simultaneously. Due to the appealing repairing effect and the promising prospect of FRP overlays in repairing fatigue

cracks, extensive experimental, analytical, and numerical research has been conducted in an attempt to answer some of the above questions. Generally, based on the considerable research advances achieved so far, *Q4* can be answered based on assumed answers to questions *Q1*, *Q2*,and *Q3*, while widely accepted and explicit answers to questions *Q1*, *Q2*, *Q3*, and *Q5* have not been reached, as explained below.

2. Analysis of cracked metallic plates with bonded FRP composite overlays

Erdogan and Arin (1972) developed an analytical solution for the fundamental model of an FRP composite-bonded cracked plate. In this model, the interfacial bond-slip relationship is assumed to be linear elastic up to debonding at a maximum shear stress/strain, and the debonding zone is assumed to coincide with the crack in the crack length direction while having an unknown extent perpendicular to the crack length direction. These two assumptions of the debonding zone together are referred to as the unknown-boundary debonding zone (UDZ) assumption in the discussions below. In addition, the model decomposes the analysis into a no-crack problem and a perturbation problem based on the principle of superposition. In the former, the crack is fully closed up by a stress at each crack face that is uniformly distributed along the crack line so that the interface near the crack is not stressed. In the latter, a uniformly distributed stress equal in magnitude to that which closes up the crack in the former is applied to open up the crack and hence the interface near the crack is stressed. This uniformly distributed stress is referred to as the crack-opening stress.

The model was then simplified by dividing the entire field into narrow strips, converting the problem into a series of one-dimensional (1D) Fredholm integral equations (Arin, 1974).

One widely adopted assumption is the no-debonding assumption which states that the interface is linear elastic without interfacial debonding. Keer et al. (1976) developed an analytical solution for the SIF of bonded FRP-overlaid cracks adopting the no-debonding assumption using the same

perturbation approach and compliance condition method. The solution is simpler but less conservative than that based on the unknown-boundary debonding assumption. An approximate method proposed by Rose (1981, 1982) also employs the perturbation approach with the no-debonding assumption. The method is based on the argument that the crack-opening stress in the perturbation problem is essentially jointly resisted by the substrate plate and the overlays, and the portion resisted by the substrate plate is responsible for the crack opening and the SIF. Instead of solving the compatibility condition to determine the sharing ratio, the model identifies two upper bound values for the SIF as explained below.

The model was subsequently extended to the analysis of cracks with an FRP overlay on only one of the two sides (i.e., single-side overlaid cracks) (Wang et al., 1998; Wang and Rose, 1999). This model is obviously rather imprecise, yet it is much simpler than the previous analytical solutions and hence has been widely adopted for evaluating the SIF of FRP-bonded metallic cracks (Jones and Peng, 2002; Clark and Romilly, 2007). Incidentally, many relatively recent analytical models for evaluating the SIF of bonded FRP-overlaid cracks that consider only stiffness-based load-sharing but not the near-crack interaction (Liu et al., 2009; Wang and Nussbaumer, 2009; Yu et al., 2013; Feng et al., 2014; Hu et al., 2016; Wang et al., 2018) are essentially equivalent to the first upper-bound method proposed by Rose (1981, 1982).

The other widely adopted assumption is the elliptical debonding zone (EDZ) assumption first proposed by Ratwani (1979) in the finite element (FE) analysis of double-side FRP-overlaid cracks. This assumption mainly follows the UDZ assumption adopted by Erdogan and Arin (1972), except that it further assumes that the debonding zone is elliptically shaped with a given aspect ratio (i.e., the extent of debonding perpendicular to the crack line is known). Colombi (2005) developed an analytical model for FRP-overlaid cracks by adopting the EDZ assumption. Specifically, it

assumes an EDZ with an aspect ratio of 0.2 and solves the compatibility condition, which is not constructed across the entire field but only along the crack line. The crack opening displacement at any point along the crack line is expressed as a function of the tensile stress in the overlay perpendicular to the crack line (referred to as the "overlay stress" hereafter), the applied stress at the far end, and the possible compressive contact stresses between the two crack faces resulting from the elastic unloading of a plastically deformed crack. Meanwhile, the corresponding displacement of the overlay due to the overlay stress (referred to as the "overlay extension" hereafter) within the debonding zone is expressed as a function of the overlay stress. The overlay extension, the interfacial slip, the overlay stress, and the crack opening displacement, all of which vary along the crack line, can be obtained simultaneously by solving the compatibility condition involving the crack opening displacement. This model provides a simpler method of constructing the compliance condition only along the crack line, which avoids the complexity of obtaining the displacements of the entire field.

While most of the abovementioned models were developed for solving double-side FRP-overlaid cracks, Ratwani (1979) proposed a method for the analysis of single-sided repairs based on the solution for double-sided repairs, in which the SIF predicted without considering out-of-plane bending is amplified by a correction factor representing the bending effect induced by the asymmetry of repair. This correction factor method was evaluated by Jones (1983) using three-dimensional (3D) FE analysis, which showed that this simple approximation method is appropriate for the analysis of single-side FRP-overlaid cracks. Thereafter, most of the proposed solutions for single-sided repairs are based on modifying the results for double-sided repairs (Wang et al., 1998; Wang and Rose, 1999; Clark and Romilly, 2007). Therefore, a solution for double-side overlaid cracks generally serves as the backbone of a solution for single-side overlaid cracks.

The accuracy of FE models for FRP-overlaid cracks is largely dependent on the modeling of interfacial properties. Following the abovementioned analytical works, most of the existing FE models have adopted either the no-debonding assumption (Liu et al., 2009; Tsouvalis et al., 2009; Yu et al., 2013, 2016; Emdad and Al-Mahaidi, 2015; Hu et al., 2016; Hosseini et al., 2017) or the EDZ assumption (Naboulsi and Mall, 1996; Sun et al., 1996; Duong and Yu, 1997; Colombi et al., 2003; Ouinas et al., 2007; Wang et al., 2014; Hu et al., 2017) to predict the SIF. In summary, in the analysis of FRP-overlaid cracks, nearly all existing models make an *a priori* assumption about the near-crack interfacial debonding zone (either no debonding zone or an EDZ), rather than have it as one of the unknowns. However, the existing experimental studies have provided compelling evidence that the assumptions regarding the interfacial behavior made in the existing models, from the linear-elastic interfacial behavior to a common shape for the debonding zone for all configurations, are questionable as discussed below. More importantly, without making the interfacial debonding zone a key unknown, it remains challenging to properly explain the mechanisms of deboning initiation and propagation and establish a thorough understanding of the behavior of FRP-overlaid cracks.

The mechanical behavior of metal-to-FRP adhesive-bonded interfaces has been extensively investigated through a succession of recent experimental and numerical studies (Xia and Teng, 2005; Fawzia et al., 2010; Colombi and Fava, 2012; Dehghani et al., 2012; Wu et al., 2012a; Yu et al., 2012; Wu et al., 2013; Yang et al., 2013; Fernando et al., 2014; Wang and Wu, 2018), which were unavailable to the earlier analytical works. In general, the local bond-slip relationship can be described by either a bi-linear or a tri-linear model, depending on the ductility of the adhesive (Yu et al., 2012; Fernando et al., 2014), as shown in Figure 2a. Both models consist of a number of distinct stages: (i) an elastic stage that is linearly ascending when $0 \leq \delta \leq \delta_1$, (ii) a plastic stage

during which the shear stress remains at τ_{max} when $\delta_1 < \delta < \delta_2$ (for the bi-linear model, $\delta_1 = \delta_2$, so a plastic stage does not exist), (iii) a softening stage that is linearly descending when $\delta_2 < \delta \leq \delta_f$, and (iv) a debonding stage with a zero shear stress when $\delta > \delta_f$ (see Appendix A for the notation). The global response model for metal-to-FRP interfaces given by Fernando et al. (2014) establishes the relationship among the interfacial shear stress distribution, the force transferred through the interface, P, and the relative displacement at the loaded end (simply referred to as the end for brevity) of the interface, Δ, (i.e., end-slip). The interfacial shear stress distributions for the bi-linear and tri-linear local relationships are illustrated in Figure 2b for increasing values of end-slip and transferred load, and the corresponding P-Δ curves are shown in Figure 2c: (i) when $P = P_1$ and $\Delta < \delta_1$, part of the bondline is in the elastic state; (ii) when $P = P_2$ and $\delta_1 < \Delta < \delta_2$, for a bi-linear model ($\delta_1 = \Delta = \delta_2$), the shear stress at the end reaches τ_{max}, and for a tri-linear model, part of the bondline close to the end is in the plastic state; (iii) when $\delta_2 < \Delta < \delta_f$ and $P = P_3$, part of the bondline close to the end is in the softening state; and (iv) when $\Delta > \delta_f$ and $P = P_4$, a debonding zone with a dimension d occurs near the end and P reaches its maximum, where δ_f is the debonding slip exceeding which debonding will occur.

Regarding the experimental observation of interfacial debonding or the lack thereof, various relatively recent technologies have made it possible. Using ultrasonic technology, the otherwise invisible interfacial debonding process between a cracked substrate plate and an FRP overlay was visualized and reported by Denney and Mall (1997). It can be inferred from the visualization that the shape of the debonding zone is not elliptical. Moreover, the interfacial debonding in an FRP-overlaid centrally-cracked plate was reported to be within a very narrow zone by Sabelkin et al. (2006), whereas the debonding zone in an FRP-overlaid edge-cracked plate was trapezoidal as reported by Huawen et al. (2010). Another study (Schubbe and Mall, 1999) undertaken using

infrared technology captured relatively superior images of the debonding zone of a series of FRP-overlaid aluminum alloy plates. A typical specimen of the study was found to have experienced no interfacial debonding even when the FRP-overlaid crack had propagated from 25 to 90 mm; debonding was only observed when the crack had propagated to 110 mm. Recently, the digital image correlation (DIC) technology, capable of appreciable accuracy in 3D displacement measurement, has also been used for strain evaluation, and as a result, it is also a suitable tool for determining the debonding zone. It was observed clearly in an FRP-overlaid edge-notched steel plate that the debonding zone did not occur when the crack length was below a threshold value, and the debonding zone shape was nearly triangular rather than elliptical (Zheng and Dawood, 2016; Zheng et al., 2018). These results together suggest that the shape of the interfacial debonding zone may be dependent on the crack geometry and the overlay configuration. They also suggest that debonding does not always coexist with the crack, and the shape of the debonding zone is often non-elliptical. Therefore, the interfacial debonding zone, including its shape and size, should be considered as an unknown for the accurate prediction of the SIF.

The most recently developed FE model (Doroudi et al., 2021) has started to treat the interfacial debonding zone as an unknown by merely specifying a local bond-slip relationship for the interface without assuming any debonding pattern. In this way, the interfacial behavior and the stress and displacement fields of the overlay and the substrate plate can be simultaneously solved from the FE model. The boundary element model developed by Hu et al. (2021) also treats the shape of the interfacial debonding zone as an unknown by assigning a local bond-slip relationship to the interface. Since the boundary element method can only simulate linear elastic behavior, the interfacial bond-slip behavior cannot be accurately simulated. Instead, it is approximated by manipulating the stiffness and the stress of the interface. The model can predict interfacial

debonding and the SIF simultaneously. While these models mark an improvement in the accuracy of prediction of interfacial behavior and the SIF, explicit answers to the questions of debonding initiation and propagation are yet to be achieved. In addition, a coupled extended-FEM (XFEM) model was used by Rashnooie et al. (2022) to predict the fatigue performance of FRP-overlaid steel cracks. In their study, the interface was simulated using a cycle-by-cycle damage model developed in a different study (Khoramishad et al., 2010) based on fatigue data of aluminum-to-aluminum single-lap joints rather than FRP-to-steel interfaces. The five questions listed earlier, except *Q*4, were not explicitly answered by their study.

The present study aims to establish a thorough understanding of the mechanical behavior of the FRP overlays-cracked metallic substrate plate system (hereafter referred to as the overlay-substrate system that includes the adhesive layer between them), with a focus on the intricate crack-overlay interaction via the adhesively-bonded interface. To this end, a new analytical model is formulated by capitalizing on the updated knowledge of metal-to-FRP interfacial behavior and the theoretical basis of the existing models. The new model employs the perturbation method to isolate the near-crack interfacial response from the interfacial behavior near the overlay ends. It includes the near-crack interfacial behavior as one of the key unknowns and defines the behavior of the interface with a proper local bond-slip relationship without assuming any *a priori* debonding pattern. In this new model, a more appropriate treatment of interfacial behavior is adopted than those in previous studies, leading to more *accurate* predictions for the crack opening displacement profile (CODP), interfacial stress distribution, and SIF. Moreover, the mechanisms of initiation and propagation of near-crack debonding are explained, and the implications of near-crack debonding on the SIF are investigated, using the proposed analytical model.

3. Basic model

3.1 The perturbation approach

The double-side FRP-overlaid cracked metallic substrate plate illustrated in Figure 3a consists of two identical overlays bonded to the plate with a relatively thin adhesive layer of constant thickness. The metallic plate contains at its center a mechanically sharp and long crack of length $2a$. The width of the substrate plate is $2w$. The overlays are a unidirectional FRP composite with the fiber direction being perpendicular to the crack line. The coordinate system has its origin at the center of the crack, with the x axis being in the direction of the crack line and the y axis being in the fiber direction of the overlays; the x-y plane is the mid-plane of the substrate plate. The bond length of an overlay, L, is measured from the end of the overlay to the crack line (x axis). Thicknesses are denoted by t, and subscripts 's' and 'o' refer, respectively, to the substrate plate and the overlays. The entire system consists of two overlays of thickness t_o bonded to a cracked substrate plate of thickness $2t_s$. For ease of discussion, the basic model is discussed with reference to a symmetric half of the system: an overlay bonded to a half-thickness substrate plate. The following assumptions are made: (i) both the substrate plate and the overlays are linear-elastic, (ii) the adhesive layers are treated as zero-thickness cohesive zones that act only in shear and are governed by a local bond-slip model, (iii) in all layers, the variation of stresses across the thickness is neglected, and (iv) the bond length of the overlays is long enough.

In the present model, a uniform tensile stress, σ, is applied at each end of the substrate plate (referred to as the 'far-end' stress), which resembles practical scenarios. The crack opening displacement, denoted by u, at any point along the crack line is defined as half of the total crack opening width there; and the profile of $u(x)$ from the crack tip to the crack mouth (where the maximum crack opening displacement is found when the crack is not overlaid) is referred to as the CODP as indicated in the figure. Interfacial stress concentrations occur in the near-crack region

① and the near-end region ② (see Figure 3a), and the main stresses in the overlay are along the *y* direction. The problem is decomposed into a no-crack problem (Figure 3b) and a perturbation problem (Figure 3c), i.e., the perturbation approach following Erdogan and Arin (1972).

3.2 The no-crack problem and near-end interfacial behavior

In the no-crack problem (Figure 3b), σ is applied to the (half-thickness) substrate plate, and a possible prestress, σ_{pre}, is applied to the overlay prior to bonding it to the substrate plate. Additionally, the crack is fully closed by a uniform stress applied at the crack face, σ_{s-} ('–' denotes closing). As a result, the substrate plate can be treated as flawless, and the interface is disturbed only in the two near-end regions ②, i.e., no interfacial stress exists in the near-crack region ①. Following the assumption that the bond length *L* is long enough, the overlay and the substrate plate have the same tensile strain in *y* direction at the crack line as follows:

$$\varepsilon_s = \varepsilon_o = \frac{\sigma t_s - \sigma_{pre} t_o}{E_s t_s + E_o t_o}, at\ y = 0 \tag{1}$$

As a result, the stress required to fully close the crack is equal to the tensile stress in the substrate plate:

$$\sigma_{s-} = E_s \varepsilon_s = \frac{\left(\sigma - t_o/t_s \cdot \sigma_{pre}\right)}{1+\rho} \tag{2}$$

where ρ is the overlay-to-substrate stiffness ratio, $\rho = E_o t_o / E_s t_s$. The overlay has a uniform tensile stress:

$$\sigma_{o,nc} = E_o \varepsilon_o = \frac{\left(t_s/t_o \sigma - \sigma_{pre}\right)}{1 + 1/\rho} \tag{3}$$

where the subscript 'nc' indicates that the overlay stress in the no-crack problem (the total overlay stress also includes the component from the perturbation problem). The total load transferred through the interface near each overlay end over a unit width is:

$$P = \frac{\left(E_o/E_s \cdot \sigma + \sigma_{pre}\right) t_o}{1+\rho} \tag{4}$$

which is solely dependent on σ and σ_{pre}. Namely, the interface near each overlay end is subjected to a load-controlled failure condition. If P is smaller than the capacity of the interface near each end of the overlay, P_u, no interfacial debonding will occur at the two overlay ends. The near-end debonding failure mode is independent of the central crack and needs to be separately addressed; it may be prevented by adopting appropriate anchorage measures (Ghafoori et al., 2012a; Hosseini et al., 2017). The present study is focused on the near-crack behavior, so the near-end interfacial behavior is not further discussed.

3.3 The perturbation problem and near-crack interfacial behavior

In the perturbation problem (Figure 3c), the crack is opened by a uniformly distributed stress applied at the crack face, σ_{s+} ('+' denotes "opening" and is omitted hereafter for simplicity) of a magnitude equal to σ_{s-}, which produces the same CODP and SIF in the substrate plate as well as the same near-crack interfacial response to those in the original problem (Figure 3a). It is resisted together by the substrate plate and overlay. The stress induced in the substrate plate is referred to as the effective crack-opening stress, $\sigma_e = \sigma_e(x)$, which is responsible for the CODP, denoted by u, and the SIF at the crack tip, K. Therefore, the CODP can be expressed as a function of the effective crack-opening stress as:

$$u = \Omega(\sigma_e) \tag{5}$$

Meanwhile, the CODP induces interfacial shear stresses and, in turn, tensile stresses in the overlay; the overlay stress $\sigma_o = \sigma_o(x)$ (for the perturbation problem only) can thus be expressed as a function of the CODP:

$$\sigma_o = \Pi(u) \tag{6}$$

Finally, the following equilibrium condition can be readily established:

$$\sigma_e t_s = \sigma_s t_s - \sigma_o t_o \tag{7}$$

By substituting Eqs. (6) and (7) into Eq. (5), the perturbation problem is mathematically described by the following implicit equation of u:

$$u = \Omega\left(\sigma_s - t_o/t_s \Pi(u)\right) \tag{8}$$

solving which requires the functions Ω and Π. Since both Ω and Π are mathematically complicated, Eq. (8) is solved numerically by dividing the cracked region, $0 \le x \le a$, into N discrete strip elements, as illustrated in the one-eighth model shown in Figures 4a and 4b considering the symmetry of the system with respect to the orthogonal planes, i.e., x-y, y-z, x-z planes. Each element is of width $b = a/N$, and spans from $y = 0$ to L. Within the i^{th} element as indicated in the figure, the crack opening displacement, u_i, overlay stress, σ_o^i, and the effective crack-opening stress, σ_e^i, are assumed to be constant.

4. Analytical solution to the perturbation problem

4.1 The weight function method

For a linear elastic isotropic body containing a crack, the SIF, $K^{(1)}$, for a load system $F^{(1)}$ can be determined from the displacement field, $u^{(2)}$, and SIF, $K^{(2)}$, for another load system $F^{(2)}$ based on either elasticity method (Bueckner, 1970) or fracture mechanics (Rice, 1972). Since the two load systems are independent, there must exist certain information unique to the cracked body for any load system, and this information is independent of any load system. This information is given through the so-called weight function (WF) as follows (Bueckner, 1970; Rice, 1972):

$$m = \frac{H}{K^{(r)}} \frac{\partial u^{(r)}}{\partial a} \tag{9}$$

where m is the WF, $H = E_s$ for a plane stress problem, and $u^{(r)}$ and $K^{(r)}$ are the displacement field and corresponding SIF induced by any reference load system denoted by '(r)', respectively. That is, m is unique to the cracked body regardless of the applied load system.

The immediate application of the WF is to determine the SIF for a load system. For a given cracked body, the WF can be determined by a known reference pair of $u^{(r)}$ and $K^{(r)}$, and for any other given load system σ^*, the SIF can be obtained from the following equation (Rice, 1972):

$$K^* = \int_{\Gamma} \sigma^* m d\Gamma + \int_{A} \sigma^* m dA \tag{10}$$

where Γ and A are the boundary and the enclosed region of the cracked body, and σ^* is the stresses (including surface tractions from the overlays in the current problem) imposed on the boundary of the cracked body. Specifically, regarding the cracked substrate plate in the current perturbation problem, the effective crack-opening stress is equivalent to the combined effect of the crack-opening stress and the interfacial shear stress (integrated as the overlay stress along the crack line) and is hence treated as a traction applied at the crack face. As a result, as long as $\sigma_e(x)$ is known, the SIF in the perturbation problem can be obtained from the following:

$$K = \int_0^a \sigma_e(x) m(a,x) dx = \int_0^a \sigma_e(x) \frac{H}{K^{(r)}} \frac{\partial u^{(r)}}{\partial a} dx \tag{11}$$

Another application of the WF is to determine the displacement field of the cracked body for a load system hence the CODP. Petroski and Achenbach (1978) used a WF-based method to calculate the CODP from the SIF by substituting the current load system for the reference load system in Eq. (11):

$$K(a)^2 = H \int_0^a \sigma_e(x) \frac{\partial u(x)}{\partial a} dx \tag{12}$$

integrating which along the crack length leads to

$$\int_0^a K(a)^2 da = H \int_0^a \sigma_e(x) u(a,x) dx \tag{13}$$

where $u(a,x)$ is the CODP corresponding to the crack of a length a. A general form for u was proposed by Petroski and Achenbach (1978) as follows to satisfy the CODP in the vicinity of the crack tip and to guarantee consistent behavior as the crack length approaches zero:

$$u(a,x) = \frac{\sigma_0}{\sqrt{2}H} \left\{ 4f\left(\frac{a}{w}\right) a^{\frac{1}{2}} (a-x)^{\frac{1}{2}} + g\left(\frac{a}{w}\right) a^{-\frac{1}{2}} (a-x)^{\frac{3}{2}} \right\} \tag{14}$$

where f is a known function while g is unknown and can be solved by substituting Eq. (14) into Eq. (13) with the solution given by Petroski and Achenbach (1978). Thereupon, the CODP is determined. Since there is one unknown, i.e., g, in this solution, it is commonly referred to as the one-condition solution to the CODP. However, it has been pointed out that this solution is not accurate for non-uniform stress distributions of $\sigma_e(x)$ (Görner et al., 1985). Then Fett et al. (1987) proposed another WF-based method (referred to as the two-condition solution) by adding an unknown to the general solution of CODP as:

$$u(a,x) = \frac{\sqrt{8}\sigma_0 a}{H} F\left(\frac{a}{W}\right)\left\{(1-x/a)^{\frac{1}{2}} + C_1(1-x/a)^{\frac{3}{2}} + C_2(1-x/a)^{\frac{5}{2}}\right\} \tag{15}$$

where C_1 and C_2 are the two unknowns. C_1 can be solved by substituting Eq. (15) into Eq. (13); C_2 can be solved by applying an additional boundary condition at the crack mouth:

$$\begin{cases} \dfrac{\partial u}{\partial x} = 0, for\ central\ cracks \\ \dfrac{\partial u^2}{\partial^2 x} = 0, for\ edge\ cracks \end{cases} \tag{16}$$

The current model adopts an approach that is more suitable for numerical integration as given below. In the current model, based on Eq. (9), the CODP can be expressed as:

$$u(a,x) = \frac{1}{E_s}\int_x^a m(a',x)K(a')da' \tag{17}$$

Further, substituting Eq. (11) into Eq. (17) leads to the following CODP as also adopted by Fett (1995) and Fett et al. (1996):

$$u(a,x) = \frac{1}{E_s}\int_0^a \int_{max(x,x')}^a m(a',x)m(a',x')\sigma_e(x')da'dx' \tag{18}$$

where x' is the position where σ_e acts. For a central crack in a finite-width plate, the weight function is given by Tada et al. (2000) as follows:

$$m(a,x)=\sqrt{\frac{2}{w}}\sqrt{tan\frac{\pi a}{2w}}\left[1-\left(\frac{cos\left(\frac{\pi a}{2w}\right)}{cos\left(\frac{\pi x}{2w}\right)}\right)^2\right]^{-1/2}\left\{1+0.297\sqrt{1-\left(\frac{x}{a}\right)^2}\left[1-cos\left(\frac{\pi a}{2w}\right)\right]\right\} \quad (19)$$

Accordingly, the crack opening displacement for the i^{th} element, u_i, is numerically obtained from the following expression:

$$u_i=\frac{1}{E_s}\sum_{j=1}^{N}\sigma_e(x_j)\int_{x_j}^{x_{j+1}}\int_{max(x,x\prime)}^{a}m(a',x_i)m(a',x')da'dx' \quad (20)$$

Substituting Eq. (19) into Eq. (20) gives the crack opening displacement for each element; the entire CODP is readily obtained by repeating the same process for all elements. Thus, $u = \Omega(\sigma_e)$ is numerically obtained.

4.2 Overlay stress

The global model of the interface established by Fernando et al. (2014) is adopted to relate the interfacial behavior to the crack opening displacement at any point along the crack line, i.e., the CODP. If the crack opening displacement is taken as the global end-slip at the interface, $\Delta = u_i$, the force transferred through the interface in the i^{th} element can be approximated by $P(u_i)\cdot b$ (the detailed relationship between P, Δ, and the interfacial shear stress distribution is given in Appendix B), and the corresponding approximate overlay stress is:

$$\bar{\sigma}_{o,i}=P(u_i)/t_o \quad (21)$$

The discrete strip element model ignores the interaction between neighboring elements, which results in a negligible error when the bonded interface between the substrate plate and the overlay is fully intact, i.e., $u_i < \delta_f$. However, the interaction must be accounted for when debonding occurs, i.e., $u_i > \delta_f$. Consequently, the function for the overlay stress is as follows:

$$\sigma_{o,i}=\Pi(u_i)=\bar{\sigma}_{o,i}-\sigma_{c,i} \quad (22)$$

where σ_c is the overlay correction stress as given in Appendix C. By substituting u_i into Eq. (22), the interfacial stress distribution $\tau_i(y)$, debonding zone length d_i, and overlay stress $\sigma_{o,i}$ can be obtained. Thus, $\sigma_o = \Pi(u)$ is numerically obtained.

4.3 Iterative solution of the implicit problem

The solution to the implicit Eq. (8) is achieved through numerical iterations as illustrated by the flowchart shown in Figure 5. At the initial step, the initial overlay stress ($\sigma_{o,i}^{(0)}$) is set to zero for all elements such that the initial effective crack-opening stress ($\sigma_{e,i}^{(0)}$) is equal to the perturbation stress (σ_s). Then the initial CODP ($u_i^{(k)}|k=0$) can be obtained from Eq. (20). This initial CODP gives the trial overlay stress ($\sigma_{o,i}^t$) and the trial effective stress ($\sigma_{e,i}^t$), from which the trial CODP (u_i^t) is obtained. The difference between the maximum trial CODP (u_{max}^t) and the maximum CODP in the k^{th} iteration ($u_{max}^{(k)}$) is compared against a tolerance. If the error is larger than the tolerance, the (k+1)th iteration is conducted with the (k+1)th effective crack-opening stress taken as the average of the trial and the k^{th} effective crack-opening stresses. Otherwise, if the error is below the tolerance, the CODP is considered converged, and both the overlay stress and the effective crack-opening stress are obtained. Thereupon, the SIF at the crack tip can be computed using the following numerical version of Eq. (11):

$$K = \sum_{i=1}^{N} \sigma_{e,i} \int_{x_i}^{x_{i+1}} m(a,x)dx \tag{23}$$

By combining the solutions to the no-crack and the perturbation problems, the entire interfacial behavior, CODP, and SIF are obtained.

4.4 Near-crack interfacial debonding is stable

In contrast to the interfacial behavior near an overlay end, the near-crack interfacial behavior is dependent on the crack opening displacement. Figure 6 shows the near-crack interfacial shear

stress distributions for increasing levels of crack opening displacements: for σ_{s1} with $u_1 < \delta_1$, the near-crack interface is in the elastic state; for σ_{s2} with $\delta_1 \leq u_2 \leq \delta_2$, the maximum interfacial shear stress is reached at the crack face; for σ_{s3} with $\delta_2 \leq u_3 \leq \delta_3$, a softening zone is developed near the crack face. Near-crack interfacial debonding occurs when $u_4 > \delta_f$ under σ_{s4}, with a debonding zone length of d_1. However, in order to increase the debonding zone length to $d_2 > d_1$, a larger crack opening displacement $u_5 > u_4$ induced by a larger crack-opening stress $\sigma_{s5} > \sigma_{s4}$ is required. The stress resisted by the substrate plate increases with the crack opening displacement, although the capacity of the interface has been reached (i.e., the overlay resistance no longer increases with the crack opening displacement). As a result, the $\sigma_s(u) - d$ diagram shown in the figure indicates that near-crack interfacial debonding is of a *stable* nature, as long as the substrate plate does not fracture. Incidentally, if the force transferred by the near-crack interface induced by the total crack-opening stress is still smaller than the capacity of the interface, $\sigma_s t_s < P_4$, the near-crack interface will remain bonded even after the complete fracture of the substrate plate. An example of such an extreme case was reported by Hosseini et al. (2017), where after the fracture of the FRP-overlaid substrate plate, the system was able to survive 28,600 fatigue cycles solely relying on the bonded interface.

5. Evaluation of the new analytical model using FE simulations

Existing experimental data from fatigue testing of FRP-overlaid cracked steel plates do not provide accurate measurements of CODP, SIF and interfacial debonding. Therefore, for the evaluation of the accuracy of the new analytical model in predicting these aspects, the analytical results are compared herein with predictions obtained from a two-dimensional (2D) FE quarter model of the FRP overlay-metallic substrate plate system using the general-purpose package ABAQUS version 2019 (Dassault Systemes, 2020).

5.1 The finite element model

Both the substrate plate (with a full thickness of $2t_s$) and the overlay (the two overlays are modeled as a single overlay with a thickness of $2t_o$) are modeled as coinciding 2D plane surfaces, as neither out-of-plane bending nor stress variation across the thickness is considered. The substrate plate is modeled as isotropic and linear-elastic with a modulus of 206 GPa representing steel. The overlay (if any) is modeled as transversely isotropic with the fiber direction (the principal direction with a much higher modulus than the other principal direction) being in the y direction and an elastic modulus of 138 GPa representing normal modulus carbon FRP (CFRP).

In the context of LEFM, the strain singularity at the crack tip for a linear elastic material is represented by $\varepsilon \propto r^{-1/2}$ (Irwin, 1957). To simulate this inverse square-root singularity, a ring of collapsed quadrilateral elements (appearing in the mesh as triangular elements sharing a common vertex) is employed to surround the crack tip, as shown in Figure 7a; their mid-side nodes on the sides connected to the crack tip are moved to the quarter-point location near the crack tip. Accordingly, the substrate plate is meshed with quadratic 8-node (linear 4-node elements do not have mid-side nodes) quadrilateral shell elements, named S8R5 in the package, with five nodal degrees of freedom (DOFs) (shell elements with six nodal DOFs and membrane elements cannot be used to evaluate SIF in the package).

The interface between the substrate plate and the overlay is simulated as a surface-based, zero-thickness cohesive zone, which can cater for the different mesh patterns of the substrate plate and the overlay (the overlay does not require a complicated focused mesh as required by the substrate plate). The interfacial shear behavior is governed by either a bilinear or trilinear bond-slip relationship as discussed above. Since the normal separation and the normal stress in the near-crack region are negligible, the interfacial Mode-I opening behavior is conveniently governed by

the same bond-slip relationship as for the shear behavior and is not further discussed in the present study; no penetration is allowed under interfacial compressive stress. The interfacial slip is the relative displacement between a node on the overlay and its corresponding projection point on the un-deformed substrate plate (at the outset of the simulation). In order to achieve a more accurate prediction of the interfacial behavior, the overlay is meshed into 8-node quadratic shell elements with six nodal DOFs as SIF evaluation is not needed (named S8R in the package). The FE model predicts the CODP, near-crack interfacial response, and the SIF at the crack tip simultaneously, without the need for assuming a priori the shape of the interfacial debonding zone near the crack.

5.2 CODP predictions for a bare plate

The accuracy of CODP predictions for bare centrally-cracked plates using the proposed analytical model, Eq. (20), is evaluated against the FE results. Figure 7a shows the quarter FE model of the centrally-cracked plate. The following boundary conditions are applied: the crack face, where $0 \le x \le a$ and $y = 0$, is free; the un-cracked part, where $a \le x \le w$ and $y = 0$, is y-symmetric; and the centerline, where $x = 0$, is x-symmetric. A uniform stress, σ, is applied to the end of the plate. Since there is no overlay, the effective crack-opening stress is equal to the far-end stress, $\sigma_e = \sigma$. The analytical and the FE predictions of the CODPs are shown in Figure 7b for different combinations of a/w and σ as indicated in the figure. The abscissa is the relative location along the crack face, and the ordinate is the crack opening displacement. The sensitivity of the analytical model to the number of strip elements is shown in the first case ($a/w = 0.5$, $\sigma = 240$ MPa), where the results for 10, 20, and 50 strip elements are seen to be basically identical. The difference in the crack mouth opening displacement ($u|_{x=0}$) between the analytical and the FE predictions is indicated in the legend for each case; all are well below 0.5%. These results altogether indicate that the analytical

model is accurate in predicting CODPs. More analytical predictions of CODPs can be found in Fett et al. (1987), Görner et al. (1985) and Petroski and Achenbach (1978).

5.3 CODP and SIF predictions for an FRP-overlaid plate

The accuracy of CODP and SIF predictions for double-side FRP-overlaid centrally-cracked plates using the new analytical model is evaluated. Figure 8a shows the one-eighth FE model consisting of the substrate plate and an overlay, whose thicknesses are t_s and t_o, respectively. A uniform stress, σ, is applied to the far-end of the substrate plate. The boundary conditions for the substrate plate are the same as those in the previous bare plate model. Figure 8b shows the boundary conditions for the overlay: y-symmetric along the crack line, where $0 \le x \le w$ and $y = 0$; x-symmetric along the centerline, where $x = 0$ and $0 \le y \le L$.

Four cases were simulated, and their parameters are listed in Table 1. The covered stiffness ratios (ρ) include 0.1, 0.17, 0.33, and 0.67, corresponding to overlay-to-substrate thickness ratios of 0.15, 0.25, 0.5, and 1, representing practically reasonable strengthening ratios. The values of a/w including 0.2, 0.3, 0.4, and 0.5, represent various degrees of damage. The far-end stresses covered are 160, 240, 320, and 400 MPa, with 160 and 400 MPa representing stress levels at service and close to yielding, respectively. It is noted that the bond length, L, was intentionally selected to be a small value to demonstrate the robustness of the new analytical model. Both the tri-linear (TL) and bi-linear (BL) interfaces were employed. Specifically, the interfacial fracture energy, G, for both cases was taken as 0.6 N/mm, which is a relatively small value (Xia and Teng, 2005; Fawzia et al., 2010; Dehghani et al., 2012; Yu et al., 2012) for a clear demonstration of the near-crack interfacial debonding process as interfacial debonding is unlikely to initiate due to a central crack when the fracture energy is sufficiently large.

To demonstrate the iterative solution process of the new analytical model, the CODPs for Case 2 (with a TL interface) under σ = 400 MPa obtained from 1, 2, 3, 6, 10, and 12 iterations are shown in Figure 8c, together with the CODP predicted by the FE model. The results indicate a rapid convergence rate of the new analytical model; the convergence was achieved within 10 iterations. The difference between the crack mouth opening displacements ($u|_{x=0}$) from the analytical and the FE models is indicated in the legend for each iteration; the difference of 3.88% for the converged result indicates good accuracy of the analytical model.

Figure 9a compares the CODP predictions for the four cases (including both the TL and the BL interfaces as indicated above each chart) under two stress levels. It is seen that the shapes of all CODPs are nearly elliptical, with larger openings for higher applied stresses. The difference between the crack mouth opening displacements predicted from the analytical and the FE models is well below 5% for all cases, as indicated in the figure. The SIFs for each case under five stress levels as predicted by both models, are displayed in Figure 9b. The differences between the analytical and the FE results are given in dashed lines against the right ordinate; all errors are well below 5%. This set of cases covering a wide range of parameters validates the accuracy of the new analytical model for CODP and SIF predictions of FRP-overlaid centrally-cracked plates.

5.4 Predictions of near-crack interfacial behavior

The accuracy of the new analytical model in predicting the shear stress distribution and the debonding zone is evaluated against the same FE model as described in the previous sub-section (Figures 8a and 8b). Both bi-linear and tri-linear types of local bond-slip relationships are considered. For each type of interface, two far-end stress levels are examined to compare the interfacial behavior. A relatively small value of ρ and a large degree of damage a/w were selected

to achieve evident near-crack debonding for demonstration purposes. The parameters for the four cases are listed in Table 2.

The near-crack interfacial shear stress contours for the bi-linear and the tri-linear cases predicted by the FE model are displayed in Figures 10a and 10b, respectively. The interface is clearly divided into four zones based on the shear stress level: *i*) the debonding zone (blue) is immediately around the center of the crack ($x = 0$, $y = 0$), where the shear stress is zero (very small stresses due to numerical errors are ignored); *ii*) the softening zone (green) encircles the debonding zone, where the stress level is below the peak stress; *iii*) the peak-stress line is represented as a narrow curved zone with a stress range of 19–20 MPa (the minimum visible range for 2D visualization) for the bi-linear interface and a wide band with a stress range of 9.9–10 MPa (an even smaller range gives identical 2D visualization) for the tri-linear interface, which is outside the softening zone; *iv*) the elastic zone (green with shade) in the outermost extends to the edges of the overlay, where the stress is below the peak stress. The boundaries of the debonding zone predicted by the analytical model are shown as black dashed curves in the contours. The analytical results coincide with the FE results for the 240 MPa stress level cases and closely match the FE results for the 400 MPa stress level cases. The detailed interfacial shear stress distributions along the centerline ($x = 0$) under 240 and 400 MPa predicted by both models are shown in Figures 10c and 10d. From $y = 0$ to 150 mm, the shear stress distribution indicates sequentially the debonding, softening, peak stress, and elastic zones. A close match between the results from the two sources is observed, indicating good accuracy of the new analytical model in predicting near-crack interfacial behavior. For both types of interfaces, the shape of the debonding zone is spindle-like, and its extent along the x-axis is shorter than the crack. A comparison of the debonding zones under the two stress levels indicates

that the process of debonding propagation is stable in both the x- and y-directions with the increase of applied load.

The overlay stress distributions along the crack line ($y = 0$) corresponding to the four cases predicted by both models are shown in Figures 10e and 10f. A close match between the results from the two sources is observed. It is noted that this overlay stress is the portion in the perturbation problem, whereas the total overlay stress is obtained by adding to it that obtained from the no-crack problem, i.e., from Eq. (3). The results indicate that, within the cracked zone ($-1 < x/a < 1$), the overlay stress is lowest at the crack tip location since there is no crack opening displacement there. Moreover, the overlay stress in the cracked zone is much higher than that outside the cracked zone, which is essentially responsible for the local crack-closing effect provided by the overlays through the bonded interface, as observed experimentally by (Ghafoori et al., 2012a). Importantly, the overlay stress within the debonding zone is lower than that at the boundary of the debonding zone (where the overlay stress peaks), and this reduction of overlay stress due to near-crack debonding increases as debonding propagates.

The above comparisons have demonstrated that the developed model is accurate in predicting the CODP, SIF, and near-crack interfacial debonding of a double-side FRP composite-overlaid metallic substrate plate with a central crack. The mechanisms of the initiation and propagation of near-crack interfacial debonding and the influence of near-crack interfacial debonding on the SIF are examined in detail through a parametric study based on the new model in the next section.

6. Evaluation of the new analytical model using experimental data

In addition to the evaluation of the analytical model conducted using FE predictions, the fatigue crack growth (FCG) curves of the analytical model are compared herein with corresponding experimental FCG curves obtained using the beach-marking technique for further evaluation of

the analytical model as the latter results are reliable. The present analytical model is for steel plates that have a central crack and are fully covered on both sides with an FRP overlay. Therefore, experimental studies to be chosen for comparison should meet the following requirements: i) the steel plates had a central crack; ii) the crack was fully covered by an FRP overlay on either side; iii) both bare and overlaid steel plates were tested; iv) the interfacial properties (i.e., bond-slip relationship) are available; and v) the material constants for FCG analysis are available. Two suitable independent experimental studies were thus selected from the published literature. Only the necessary details of the experiments are presented here, but further details can be found in Hu et al. (2021) and Wang et al. (2015). Both studies used a ductile adhesive (i.e., Araldite 2015), for which a tri-linear local bond-slip relationship was first proposed by Yu et al. (2012) based on an experimental study. While Wang et al. (2015) did not consider the behavior of the interface in their numerical analysis, Hu et al. (2021) adopted the tri-linear local bond-slip model in their boundary-element model (BEM). The values of the model parameters in the BEM of Hu et al. (2021) were taken from another experimental study (Pang 2019) on the bond-slip relationship between CFRP and steel with Araldite 2015 at the interface, and the values were reasonably close to the values proposed by Yu et al. (2012). Therefore, in the present study, the tri-linear bond-slip model was used for the interface with the same parameter values as used by Hu et al. (2021) to predict the FCG curves for both studies.

The prediction of FCG curves was achieved by calculating the SIFs using the present analytical model at increasing crack lengths and then obtaining the corresponding numbers of fatigue cycles through a Paris law-like crack growth model, as detailed in Hu et al. (2021) and Wang et al. (2015) . In the referenced studies, different crack growth equations were adopted with different crack growth constants, i.e., C and m. In the present study, the analytical model was used to calculate

the SIFs at various crack lengths, and the equations used in the respective studies were then used to obtain the FCG curves. The values of the parameters used in the analytical model for the two studies are listed in Table 3. The comparisons between the analytical results and experimental data for the two studies are presented in Figure 11a for Wang et al. (2015) and 11b for Hu et al. (2021). A close match between the predictions and the experimental data can be seen for both experimental studies.

7 The mechanism and influence of near-crack interfacial debonding

7.1 The initiation and propagation mechanisms

Two examples were analyzed using the new analytical model to investigate the initiation and propagation mechanisms of near-crack interfacial debonding. In the first example, the crack length is unchanged while the substrate plate is subjected to applied far-end stresses of 150, 250, and 350 MPa, representing the increase of load; in the second, the same far-end stress is applied to crack lengths of 20, 30, and 45 mm, representing crack propagation. The values of the model parameters are summarized in Table 5.

The CODP (shown as blue dashed curves) and the corresponding near-crack interfacial debonding boundary (shown as red zones) for the first example are presented in Figure 12a. When σ=150 MPa, there is no interfacial debonding because the CODP along the entire crack is smaller than the debonding initiation slip, i.e., $u < \delta_f$, as indicated by the black dashed lines in the figure. When σ increases to 250 MPa, a spindle-shaped debonding zone appears within the region where $u > \delta_f$, as shown in the figure. Increasing σ further to 350 MPa results in the enlargement of CODP and hence the propagation of the debonding zone in both the x and y directions. The extent of the debonding zone in the x direction is always shorter than the crack, because $u = 0 < \delta_f$ at the crack tip. These results indicate that at low-stress levels when the induced CODP is smaller than the

debonding initiation slip, there is no interfacial debonding. When the stress level is large enough to induce crack opening displacements exceeding the debonding initiation slip, debonding initiates. Further increases in the stress level lead to the widening of the crack and hence the propagation of debonding.

For the second example, the CODP and the near-crack interfacial debonding zones are presented in Figure 12b. Debonding does not initiate when a = 20 mm because $u < \delta_f$ as shown in the figure. With the increase of the crack length to a = 30 mm, a small debonding zone appears within the region where $u > \delta_f$. When the crack length increases to a = 45 mm, the debonding zone attains a considerable size in both the x and y directions. This set of results indicates that, under a constant stress level, when the crack length is small and the CODP is smaller than the debonding initiation slip, there is no interfacial debonding. When the crack length is large enough to induce crack opening displacements exceeding the debonding initiation slip, debonding initiates. Further increases in the crack length lead to the widening of the crack and hence the propagation of debonding.

Put together, the initiation and propagation mechanisms of near-crack interfacial debonding can be summarized as follows: (*i*) interfacial debonding initiates only when the crack opening displacement exceeds the debonding initiation slip, which is an interfacial parameter; (*ii*) with either or both of a load increase and crack propagation, the crack opening displacement increases, enlarging the debonding zone; (*iii*) the shape of the debonding zone is dependent on the shape of the CODP, and thus the shape will be different for different substrate plate and overlay parameters and different crack locations; and (*iv*) since the crack opening displacement at the crack tip is zero, the debonding zone is always shorter than the crack in the crack line direction.

This account of the interfacial debonding mechanism is compatible with the experimental observation that debonding does not occur as a result of the mere presence of an underlying crack (Schubbe and Mall, 1999). Instead, it only occurs when the crack opening displacement exceeds the debonding initiation slip. Also, it is compatible with the observation that the extent of the near-crack debonding zone along the crack line is shorter than the crack length (Zheng and Dawood, 2016; Hu et al., 2021), since the crack opening displacement near the crack tip is smaller than the debonding initiation slip. Moreover, the shape of the debonding zone can be non-elliptical due to different shapes of the CODPs, as a result of different substrate plate and overlay parameters (Sabelkin et al., 2006; Huawen et al., 2010; Zheng and Dawood, 2016).

7.2 Influence of near-crack interfacial debonding on the SIF

The new analytical model was deployed to conduct a parametric study to investigate the influence of near-crack interfacial debonding on the SIF, and the results are presented in this section. The behavior of an FRP overlay-metallic substrate system with the same overlays, substrate, and far-end stress of 300 MPa is examined for four types of interfaces (IFs) (hereafter referred to as IF-A, IF-B, IF-C and IF-D in the order of increasing debonding slips). IFs-A, B and C represent bonded interfaces formed with a relatively stiff but brittle adhesive; they have a bi-linear bond-slip response and the same interfacial stiffness. IF-D represents an interface formed with a softer and more ductile adhesive having a tri-linear bond-slip response (Figure 13a). Based on the mechanisms of near-crack interfacial debonding as discussed above, the stiffer interface is more prone to near-crack interfacial debonding. Therefore, by comparing the behaviors of the system with these two different types of interfaces, the influence of near-crack interfacial debonding on the SIF can be investigated.

In order to make the predictions more realistic, the properties of interfaces B and D were assumed with reference to existing experimental data (Xia and Teng, 2005; Yu et al., 2012). IF-A and IF-C were given smaller or larger values of τ_{max} and the corresponding δ_f than those of IF-B to achieve a more nuanced understanding of the influence of near-crack debonding. The values of model parameters for the overlay-substrate system including the four interfaces are summarized in Table 5. The bond-slip curves of the four interfaces are given in Figure 13a. It shows that IF-D is much more ductile than the other three, which all have the same stiffness but different maximum shear stresses and debonding slips.

With each interface, the predicted near-crack debonding zones of the system at crack lengths of 5, 10, 20, 30, 40, and 50 mm are shown in Figures 13d, 13e, and 13f. For the least ductile interface (i.e., IF-A), when the crack length is smaller than 20 mm, there is no near-crack debonding; when the crack length reaches 30 mm, near-crack debonding has occurred over a small zone, and this zone expands as the crack length increases, resulting in a considerable debonding zone at a 50-mm crack length (Figure 13d) with its maximum half-width (perpendicular to the crack) exceeding 25 mm. For the realistic bi-linear interface (i.e., IF-B), near-crack debonding does not occur when the crack length reaches 40 mm, and only a relatively small near-crack debonding zone (with its half-width being around 9 mm) has developed when the crack length reaches 50 mm, see Figure 13e. For the two more ductile interfaces (IF-C and IF-D), no interfacial debonding has occurred up to a crack length of 50 mm, see Figure 13f. These four series of predictions show a spectrum from a considerable near-crack debonding zone to no debonding for the same overlay-substrate system (except for differences in the interface) under the same loading.

The predicted SIFs for the four interface types at 31 crack lengths (at 0.5-mm intervals for crack lengths of 5 – 10 mm and at 2-mm intervals for crack lengths of 10 – 50 mm) are shown in Figure

13b, and the SIFs of the bare metallic plate as a baseline are also provided. It is seen that the four interfaces result in quite similar SIFs, which are all much smaller than those of the bare plate. This observation indicates that, for these four cases, with or without the presence of near-crack debonding, the FRP overlays provide effective SIF reductions and lead to similar SIFs. Moreover, it shows that IF-A and IF-B (with the presence of near-crack debonding) result in smaller SIFs than IF-D (without the presence of near-crack debonding), due to the higher interfacial stiffness of the former two interfaces despite the presence of debonding. A comparison of the results obtained with IF-A, IF-B and IF-C shows the effect of debonding on the SIF, and this effect is rather moderate.

A fatigue crack growth analysis of the system was conducted for the four interfaces, using fatigue constants of $C = 3.38 \times 10^{-14}$ and $m = 3.29$ as measured by Zheng and Dawood (2016), a stress ratio of 0.1, and a fracture toughness of 2500 MPa mm$^{1/2}$. The predicted crack length-fatigue life (*a*-*N*) curves of the overlay-substrate system for the four interfaces as well as that of the bare plate are shown in Figure 13c. The four interfaces give generally similar fatigue lives that are much longer than that of the bare plate. More specifically, the fatigue lives of the system with IF-A, IF-B and IF-C are quite similar despite their very different debonding zone sizes, and they are higher than that with IF-D.

These observations are contradictory to the conclusion that near-crack debonding significantly reduces the benefit of FRP overlays (Colombi et al., 2003; Colombi and Fava, 2015), which seems to have received wide support in the existing literature (e.g., Kaan et al. 2012; Wu et al. 2012b; El-Emam et al. 2016; Hu et al. 2017; Lepretre et al. 2018; Doroudi et al. 2021; Hassan et al. 2021). It has been numerically demonstrated that a larger near-crack debonding zone leads to a higher SIF in previous studies (Colombi et al., 2003; Zheng and Dawood, 2016). However, this cannot

and should not be taken to directly imply that near-crack debonding significantly reduces the benefit of FRP overlays regardless of the other parameters of the interface; instead, it only indicates that it is important to use an accurate debonding zone in making such predictions (i.e., assuming a larger or smaller debonding zone than the 'true' one will lead to inaccurate SIF predictions).

In reality, for each overlay-substrate system under a given load and at a certain crack length, there is a unique debonding zone (or no debonding) with a corresponding SIF, without other choices. The proposed model can accurately predict the unique debonding zone and the SIF, and the results have shown that there is no direct correlation between the presence of a near-crack debonding zone and the value of SIF. Instead, the SIF is uniquely determined by the geometric and material properties of the overlay-substrate system (including those of the interface), together with the crack length and the loading condition. Near-crack debonding itself or the lack thereof is an *outcome* as much as the SIF is an outcome of the overlay-substrate system with a given crack length and subjected to a given load level, rather than a *cause* that influences the SIF. The near-crack debonding and the SIF are an equal pair determined simultaneously by the properties of the system together with the crack length and the loading condition. Therefore, given the fact that near-crack debonding is a stable phenomenon that does not cause the failure of the repair like near-end debonding, it may be reasonable to consider near-crack debonding as a relatively mild phenomenon. It is noted that these comments are based on the assumption that the overlay-substrate system does not suffer additional damage from fatigue loading.

8. Concluding remarks

A new analytical model for the problem of near-crack interfacial debonding (or simply near-crack debonding) in a centrally-cracked metallic plate bonded with FRP composite overlays on both sides has been presented. The model employs the weight function method to establish the link

between the crack opening displacement profile and the resistance offered by the substrate plate, and utilizes the interfacial response model to relate the crack opening displacement profile with the resistance offered by the overlays. By solving the equilibrium equation along the crack line, the crack opening displacement profile, the near-crack interfacial response, and the stress intensity factor are all obtained simultaneously. The performance of the new analytical model has been evaluated against results from FE simulations and experimental studies. The close match between the analytical and the FE and experimental results demonstrates the accuracy of the analytical model.

Near-crack debonding has been shown to be independent of the mere presence of an underlying crack; instead, it depends on the crack opening displacement of the underlying crack. Near-crack debonding initiates when the crack opening displacement exceeds the debonding initiation slip, and will then enter a stable propagation process with the increase of the applied load or with the propagation of the crack length, both of which increase the crack opening displacement. This debonding only moderately reduces the stress level in the overlays covering the near-crack debonding zone; namely, the strengthening effect of the overlays is mostly preserved despite the presence of near-crack debonding.

Moreover, numerical results presented in the paper have demonstrated that, for FRP overlay-cracked metallic substrate plate systems which are identical except for the use of different bonding adhesives (i.e., different interface types), it is possible for an interface with near-crack debonding to achieve a better repairing effect than one without near-crack debonding. This is because near-crack debonding is only a moderate factor among several other factors that influence the value of SIF.

Furthermore, it should be borne in mind that near-crack debonding is as much an outcome as the stress intensity factor rather than a cause to the repairing effect; they are both uniquely determined by the geometric and material properties of the overlay-substrate system, the crack length (which also depends on the fatigue loading process) and the imposed load level. Therefore, due to the stable nature and the mild consequences, near-crack debonding may, after all, be considered a *benign* phenomenon.

It is suggested that in the design of FRP overlays for repairing fatigue damage, near-crack debonding should cause no special concern as long as the bond length is sufficient to accommodate its propagation and its effect is included in the SIF prediction. The findings of the present study imply that a combination of adhesive bonding throughout the interface with mechanical fixtures to suppress near-end debonding may lead to the maximum repairing effect. Therefore, for fatigue-repair systems using pre-stressed unbonded FRP overlays (e.g., Hosseini et al., 2017, 2019), the required pre-stressing level to achieve the same repairing effect could be reduced or an enhanced repairing effect could be achieved if the overlays are adhesively bonded to the substrate.

The proposed model provides a basic building block for developing an in-depth understanding of the benefit of FRP repair against fatigue damage in a broad area. Although it is developed for central cracks, the solutions for single- and double-edged cracks can be readily obtained by substituting the relevant equations with those for edge cracks. Similarly, the solution for single-side FRP-overlaid cracks can be developed based on the current model using the bending correction factor method. . It should also be noted that while the study was conducted with explicit reference to metallic plates bonded with FRP overlays, the analytical model is applicable to combinations of other materials as long as the substrate plate material is isotropic, and both components remain linear-elastic during the loading process.

Funding: This work was supported by the Research Grants Council (RGC) of the Hong Kong Special Administrative Region, China (Project No.: T22-502/18-R).

References

Aljabar, N.J., Zhao, X.L., Al-Mahaidi, R., Ghafoori, E., Motavalli, M., Koay, Y.C., 2017. Fatigue tests on UHM-CFRP strengthened steel plates with central inclined cracks under different damage levels. Composite Structures 160, 995–1006. https://doi.org/10.1016/j.compstruct.2016.10.122

Arin, K., 1974. A plate with a crack, stiffened by a partially debonded stringer. Engineering Fracture Mechanics 6, 133–140. https://doi.org/10.1016/0013-7944(74)90052-6

Bueckner, H., 1970. Novel principle for the computation of stress intensity factors. Z Angew Math Mech 50, 529–546.

Clark, R.J., Romilly, D.P., 2007. Linear coupled bending and extension of an unbalanced bonded repair. International Journal of Solids and Structures 44, 3156–3176. https://doi.org/10.1016/j.ijsolstr.2006.09.012

Colombi, P., 2005. Plasticity induced fatigue crack growth retardation model for steel elements reinforced by composite patch. Theoretical and Applied Fracture Mechanics 43, 63–76. https://doi.org/10.1016/j.tafmec.2004.12.003

Colombi, P., Bassetti, A., Nussbaumer, A., 2003. Crack growth induced delamination on steel members reinforced by prestressed composite patch. Fatigue and Fracture of Engineering Materials and Structures 26, 429–437. https://doi.org/10.1046/j.1460-2695.2003.00642.x

Colombi, P., Fava, G., 2016. Fatigue crack growth in steel beams strengthened by CFRP strips. Theoretical and Applied Fracture Mechanics 85, 173–182. https://doi.org/10.1016/j.tafmec.2016.01.007

Colombi, P., Fava, G., 2015. Experimental study on the fatigue behaviour of cracked steel beams repaired with CFRP plates. Engineering Fracture Mechanics 145, 128–142. https://doi.org/10.1016/j.engfracmech.2015.04.009

Colombi, P., Fava, G., 2012. Fatigue behaviour of tensile steel/CFRP joints. Composite Structures 94, 2407–2417. https://doi.org/10.1016/j.compstruct.2012.03.001

Colombi, P., Fava, G., Sonzogni, L., 2015. Fatigue crack growth in CFRP-strengthened steel plates. Composites Part B: Engineering 72, 87–96. https://doi.org/10.1016/j.compositesb.2014.11.036

Dassault Systemes, 2020. ABAQUS: Theory and User's manuals.

Dehghani, E., Daneshjoo, F., Aghakouchak, A.A., Khaji, N., 2012. A new bond-slip model for adhesive in CFRP-steel composite systems. Engineering Structures 34, 447–454. https://doi.org/10.1016/j.engstruct.2011.08.037

Deng, J., Fei, Z., Li, J., & Li, H. (2023). Fatigue behaviour of notched steel beams strengthened by a self-prestressing SMA/CFRP composite. Engineering Structures, 274. https://doi.org/10.1016/j.engstruct.2022.115077

Denney, J.J., Mall, S., 1997. Characterization of disbond effects on fatigue crack growth behavior in aluminum plate with bonded composite patch. Engineering Fracture Mechanics 57, 507–525. https://doi.org/10.1016/S0013-7944(97)00050-7

Domazet, Ž., 1996. Comparison of fatigue crack retardation methods. Engineering Failure Analysis 3, 137–147. https://doi.org/10.1016/1350-6307(96)00006-4

Doroudi, Y., Fernando, D., Hosseini, A., Ghafoori, E., 2021. Behavior of cracked steel plates strengthened with adhesively bonded CFRP laminates under fatigue Loading: Experimental

and analytical study. Composite Structures 266, 113816. https://doi.org/10.1016/j.compstruct.2021.113816

Duong, C.N., Yu, J., 1997. The stress intensity factor for a cracked stiffened sheet repaired with an adhesively bonded composite patch. International Journal of Fracture 84, 37–60. https://doi.org/10.1023/A:1007368030354

Elber, W., 1971. The significance of fatigue crack closure. Damage Tolerance in Aircraft Structures ASTM STP 486 230–242.

El-Emam, H.M., Salim, H.A., Sallam, H.E.-D.M., 2016. Composite patch configuration and prestraining effect on crack tip deformation and plastic zone for inclined cracks. Journal of Composites for Construction 20, 04016002. https://doi.org/10.1061/(asce)cc.1943-5614.0000655

Emdad, R., Al-Mahaidi, R., 2015. Effect of prestressed CFRP patches on crack growth of centre-notched steel plates. Composite Structures 123, 109–122. https://doi.org/10.1016/j.compstruct.2014.12.007

Erdogan, F., Arin, K., 1972. A sandwich plate with a part-through and a debonding crack. Engineering Fracture Mechanics 4, 449–458. https://doi.org/10.1016/0013-7944(72)90057-4

Fawzia, S., Zhao, X.L., Al-Mahaidi, R., 2010. Bond-slip models for double strap joints strengthened by CFRP. Composite Structures 92, 2137–2145. https://doi.org/10.1016/j.compstruct.2009.09.042

Feng, P., Hu, L., Zhao, X.L., Cheng, L., Xu, S., 2014. Study on thermal effects on fatigue behavior of cracked steel plates strengthened by CFRP sheets. Thin-Walled Structures 82, 311–320. https://doi.org/10.1016/j.tws.2014.04.015

Fernando, D., Yu, T., Teng, J.G., 2014. Behavior of CFRP laminates bonded to a steel substrate using a ductile adhesive. Journal of Composites for Construction 18, 04013040. https://doi.org/10.1061/(ASCE)CC.1943-5614.0000439

Fett, T., 1995. Evaluation of the bridging relation from crack-opening-displacement measurements by use of the weight function. Journal of the American Ceramic Society 78, 945–948. https://doi.org/10.1111/j.1151-2916.1995.tb08419.x

Fett, T., Mattheck, C., Munz, D., 1987. On the calculation of crack opening displacement from the stress intensity factor. Engineering Fracture Mechanics 27, 697–715. https://doi.org/10.1016/0013-7944(87)90159-7

Fett, T., Munz, D., Seidel, J., Stech, M., Rodel, J., 1996. Correlation between long and short crack r-curves in alumina using the crack opening displacement and fracture mechanical weight function approach. Journal of the American Ceramic Society 79, 1189–1196. https://doi.org/10.1111/j.1151-2916.1996.tb08571.x

Fisher, John W., Kaufmann, E.J., Pense, A.W., 1998. Effect of corrosion on crack development and fatigue life. Transportation Research Record: Journal of the Transportation Research Board 1624, 110–117. https://doi.org/10.3141/1624-13

Fisher, John W, Kulak, G.L., Smith, I.F.C., 1998. A fatigue primer for structural engineers. National Steel Bridge Alliance, American Institute of Steel Construction.

France, E.J., 2019. The Alexander L. Kielland disaster revisited: a review by an experienced welding engineer of the catastrophic north sea platform collapse. Journal of Failure Analysis and Prevention 19, 875–881. https://doi.org/10.1007/s11668-019-00680-4

Ghafoori, E., Motavalli, M., Botsis, J., Herwig, A., Galli, M., 2012a. Fatigue strengthening of damaged metallic beams using prestressed unbonded and bonded CFRP plates. International Journal of Fatigue 44, 303–315. https://doi.org/10.1016/j.ijfatigue.2012.03.006

Ghafoori, E., Schumacher, A., Motavalli, M., 2012b. Fatigue behavior of notched steel beams reinforced with bonded CFRP plates: Determination of prestressing level for crack arrest. Engineering Structures 45, 270–283. https://doi.org/10.1016/j.engstruct.2012.06.047

Görner, F., Mattheck, C., Morawietz, P., Munz, D., 1985. Limitations of the Petroski-Achenbach crack opening displacement approximation for the calculation of weight functions. Engineering Fracture Mechanics 22, 269–277. https://doi.org/10.1016/S0013-7944(85)80029-1

Hassan, M.M., Shafiq, M.A., Mourad, S.A., 2021. Experimental study on cracked steel plates with different damage levels strengthened by CFRP laminates. International Journal of Fatigue 142, 105914. https://doi.org/10.1016/j.ijfatigue.2020.105914

Hmidan, A., Kim, Y.J., Yazdani, S., 2014. Stress intensity factors for cracked steel girders strengthened with CFRP sheets. Journal of Composites for Construction 19, 1–12. https://doi.org/10.1061/(ASCE)CC.1943-5614.0000552.

Hosseini, A., Ghafoori, E., Motavalli, M., Nussbaumer, A., Zhao, X., 2017. Mode I fatigue crack arrest in tensile steel members using prestressed CFRP plates. Composite Structures 178, 119–134. https://doi.org/10.1016/j.compstruct.2017.06.056

Hosseini, A., Nussbaumer, A., Motavalli, M., Zhao, X.L., Ghafoori, E., 2019. Mixed mode I/II fatigue crack arrest in steel members using prestressed CFRP reinforcement. International Journal of Fatigue 127, 345–361. https://doi.org/10.1016/j.ijfatigue.2019.06.020

Hu, L., Feng, P., Zhao, X., 2017. Fatigue design of CFRP strenghened steel members. Thin Walled Structures 119, 482–498. https://doi.org/10.1016/j.tws.2017.06.029

Hu, L., Wang, Y., Feng, P., Wang, H., Qiang, H., 2021. Debonding development in cracked steel plates strengthened by CFRP laminates under fatigue loading: Experimental and boundary element method analysis. Thin-Walled Structures 166, 108038. https://doi.org/10.1016/j.tws.2021.108038

Hu, L.L., Zhao, X.L., Feng, P., 2016. Fatigue behavior of cracked high-strength steel plates strengthened by CFRP sheets. Journal of Composites for Construction 1–10. https://doi.org/10.1061/(ASCE)CC.1943-5614.0000698.

Huawen, Y., König, C., Ummenhofer, T., Shizhong, Q., Plum, R., 2010. Fatigue performance of tension steel plates strengthened with prestressed CFRP laminates. Journal of Composites for Construction 14, 609–615. https://doi.org/10.1061/(ASCE)CC.1943-5614.0000111

Invernizzi, S., Montagnoli, F., Carpinteri, A., 2022. Very high cycle corrosion fatigue study of the collapsed polcevera bridge, Italy. Journal of Bridge Engineering 27, 1–13. https://doi.org/10.1061/(asce)be.1943-5592.0001807

Irwin, G.R., 1957. Analysis of stresses and strains near the end of a crack traversing a plate. Journal of Applied Mechanics.

Jiang, F., Ding, Y., Song, Y., Geng, F., & Wang, Z. (2022). CFRP strengthening of fatigue cracks at U-rib to diaphragm welds in orthotropic steel bridge decks: Experimental study, optimization, and decision-making. Structures, 43, 1216–1229. https://doi.org/10.1016/j.istruc.2022.07.039

Jiao, H., Mashiri, F., Zhao, X.L., 2012. A comparative study on fatigue behaviour of steel beams retrofitted with welding, pultruded CFRP plates and wet layup CFRP sheets. Thin-Walled Structures 59, 144–152. https://doi.org/10.1016/j.tws.2012.06.002

Jones, R., 1983. Neutral axis offset effects due to crack patching. Composite Structures 1, 163–174. https://doi.org/10.1016/0263-8223(83)90010-7

Jones, R., Peng, D., 2002. A simple method for computing the stress intensity factors for cracks at notches. Engineering Failure Analysis 9, 683–702. https://doi.org/10.1016/S1350-6307(02)00007-9

Jones, S.C., Civjan, S.A., 2003. Application of fiber reinforced polymer overlays to extend steel fatigue life. Journal of Composites for Construction 7, 331–338. https://doi.org/10.1061/(ASCE)1090-0268(2003)7:4(331)

Kaan, B.N., Alemdar, F., Bennett, C.R., Matamoros, A., Barrett-Gonzalez, R., Rolfe, S., 2012. Fatigue enhancement of welded details in steel bridges using CFRP overlay elements. Journal of Composites for Construction 16, 138–149. https://doi.org/10.1061/(asce)cc.1943-5614.0000249

Keer, L., Lin, C., Mura, T., 1976. Fracture analysis of adhesively bonded sheets. Journal of Applied Mechanics 43, 652–656. https://doi.org/10.1115/1.3423949

Khoramishad, H., Crocombe, A. D., Katnam, K. B., & Ashcroft, I. A. (2010). Predicting fatigue damage in adhesively bonded joints using a cohesive zone model. International Journal of Fatigue, 32(7), 1146–1158. https://doi.org/10.1016/j.ijfatigue.2009.12.013

Lepretre, E., Chataigner, S., Dieng, L., Gaillet, L., 2018. Fatigue strengthening of cracked steel plates with CFRP laminates in the case of old steel material. Construction and Building Materials 174, 421–432. https://doi.org/10.1016/j.conbuildmat.2018.04.063

Liu, H., Xiao, Z., Zhao, X.L., Al-Mahaidi, R., 2009. Prediction of fatigue life for CFRP-strengthened steel plates. Thin-Walled Structures 47, 1069–1077. https://doi.org/10.1016/j.tws.2008.10.011

Mall, S., Conley, D.S., 2009. Modeling and validation of composite patch repair to cracked thick and thin metallic panels. Composites Part A: Applied Science and Manufacturing 40, 1331–1339. https://doi.org/10.1016/j.compositesa.2008.08.007

Naboulsi, S., Mall, S., 1996. Modeling of a cracked metallic structure with bonded composite patch using the three layer technique. Composite Structures 35, 295–308. https://doi.org/10.1016/0263-8223(96)00043-8

Ouinas, D., Bouiadjra, B.B., Serier, B., 2007. The effects of disbonds on the stress intensity factor of aluminium panels repaired using composite materials. Composite Structures 78, 278–284. https://doi.org/10.1016/j.compstruct.2005.10.012

Pang, Y., 2019. Study on the Bond Behavior of CFRP-Steel Interfaces under Extreme Service Environment (Doctor Thesis), Southeast University, Nanjing, China.

Paris, P., Erdogan, F., 1963. A critical analysis of crack propagation laws. Journal of Basic engineering Transactions ASME. https://doi.org/10.1115/1.3656900

Petroski, H.J., Achenbach, J.D., 1978. Computation of the weight function from a stress intensity factor. Engineering Fracture Mechanics 10, 257–266. https://doi.org/10.1016/0013-7944(78)90009-7

Rashnooie, R., Zeinoddini, M., Ahmadpour, F., Beheshti Aval, S. B., & Chen, T. (2022). A coupled XFEM fatigue modelling of crack growth, delamination and bridging in FRP strengthened metallic plates. Engineering Fracture Mechanics, 109017. https://doi.org/10.1016/j.engfracmech.2022.109017

Ratwani, M., 1979. Analysis of cracked, adhesively bonded laminated structures. AIAA journal 17, 988–994. https://doi.org/10.2514/3.61263

Razavi, S.M.J., Ayatollahi, M.R., Sommitsch, C., Moser, C., 2017. Retardation of fatigue crack growth in high strength steel S690 using a modified stop-hole technique. Engineering Fracture Mechanics 169, 226–237. https://doi.org/10.1016/j.engfracmech.2016.11.013

Rice, J.R., 1972. Some remarks on elastic crack-tip stress fields. International Journal of Solids and Structures 8, 751–758. https://doi.org/10.1016/0020-7683(72)90040-6

Rodríguez-Sánchez, J.E., Rodríguez-Castellanos, A., Pérez-Guerrero, F., Carbajal-Romero, M.F., Liu, S., 2011. Offshore fatigue crack repair by grinding and wet welding. Fatigue and Fracture of Engineering Materials and Structures 34, 487–497. https://doi.org/10.1111/j.1460-2695.2010.01541.x

Rose, L.R.F., 1982. A cracked plate repaired by bonded reinforcements. International Journal of Fracture 18, 135–144. https://doi.org/10.1007/BF00019638

Rose, L.R.F., 1981. An application of the inclusion analogy for bonded reinforcements. International Journal of Solids and Structures 17, 827–838. https://doi.org/10.1016/0020-7683(81)90091-3

Sabelkin, V., Mall, S., Avram, J.B., 2006. Fatigue crack growth analysis of stiffened cracked panel repaired with bonded composite patch. Engineering Fracture Mechanics 73, 1553–1567. https://doi.org/10.1016/j.engfracmech.2006.01.029

Schubbe, J.J., Mall, S., 1999. Investigation of a cracked thick aluminum panel repaired with a bonded composite patch. Engineering Fracture Mechanics 63, 305–323. https://doi.org/10.1016/S0013-7944(99)00032-6

Shin, C.S., Wang, C.M., Song, P.S., 1996. Fatigue damage repair: A comparison of some possible methods. International Journal of Fatigue 18, 535–546. https://doi.org/10.1016/S0142-1123(96)00029-1

Sun, C.T., Klug, J., Arendt, C., 1996. Analysis of cracked aluminum plates repaired with bonded composite patches. AIAA Journal 34, 369–374. https://doi.org/10.2514/3.13073

Tada, H., Paris, P.C., Irwin, G.R., 2000. The stress analysis of cracks handbook, Third Edition. https://doi.org/10.1115/1.801535

Tavakkolizadeh, M., Saadatmanesh, H., 2003. Fatigue strength of steel girders strengthened with carbon fiber reinforced polymer patch. Journal of Structural Engineering 129, 186–196. https://doi.org/10.1061/(ASCE)0733-9445(2003)129:2(186)

Teng, J.G., Yu, T., Fernando, D., 2012. Strengthening of steel structures with fiber-reinforced polymer composites. Journal of Constructional Steel Research 78, 131–143. https://doi.org/10.1016/j.jcsr.2012.06.011

Tsouvalis, N.G., Mirisiotis, L.S., Dimou, D.N., 2009. Experimental and numerical study of the fatigue behaviour of composite patch reinforced cracked steel plates. International Journal of Fatigue 31, 1613–1627. https://doi.org/10.1016/j.ijfatigue.2009.04.006

Wang, C.H., Rose, L.R.F., 1999. A crack bridging model for bonded plates subjected to tension and bending. International Journal of Solids and Structures 36, 1985–2014. https://doi.org/10.1016/S0020-7683(98)00070-5

Wang, C.H., Rose, L.R.F., Callinan, R., 1998. Analysis of out-of-plane bending in one-sided bonded repair. International Journal of Solids and Structures 35, 1653–1675. https://doi.org/10.1016/S0020-7683(97)00129-7

Wang, H.T., Wu, G., 2018. Bond-slip models for CFRP plates externally bonded to steel substrates. Composite Structures 184, 1204–1214. https://doi.org/10.1016/j.compstruct.2017.10.033

Wang, H.T., Wu, G., Pang, Y.Y., 2018. Theoretical and numerical study on stress intensity factors for FRP-strengthened steel plates with double edge cracks. Sensors 1–19. https://doi.org/10.3390/s18072356

Wang, H.T., Wu, G., Wu, Z.S., 2014. Effect of FRP configurations on the fatigue repair effectiveness of cracked steel plates. Journal of Composites for Construction 18, 04013023. https://doi.org/10.1061/(ASCE)CC.1943-5614.0000422

Wang, R., Nussbaumer, A., 2009. Modelling fatigue crack propagation of a cracked metallic member reinforced by composite patches. Engineering Fracture Mechanics 76, 1277–1287. https://doi.org/10.1016/j.engfracmech.2009.02.004

Wu, C., Zhao, X., Duan, W.H., Al-Mahaidi, R., 2012a. Bond characteristics between ultra high modulus CFRP laminates and steel. Thin-Walled Structures 51, 147–157. https://doi.org/10.1016/j.tws.2011.10.010

Wu, C., Zhao, X.L., Al-Mahaidi, R., Emdad, M., Duan, W., 2012b. Fatigue tests of cracked steel plates strengthened with UHM CFRP plates. Advances in Structural Engineering 15, 1801–1816. https://doi.org/10.1260/1369-4332.15.10.1801

Wu, C., Zhao, X.L., Chiu, W.K., Al-Mahaidi, R., Duan, W.H., 2013. Effect of fatigue loading on the bond behaviour between UHM CFRP plates and steel plates. Composites Part B: Engineering 50, 344–353. https://doi.org/10.1016/j.compositesb.2013.02.040

Wu, G., Wang, H.T., Wu, Z.S., Liu, H.Y., Ren, Y., 2012. Experimental study on the fatigue behavior of steel beams strengthened with different fiber-reinforced composite plates.

Journal of Composites for Construction 16, 127–137. https://doi.org/10.1061/(ASCE)CC.1943-5614.0000243

Xia, S.H., Teng, J.G., 2005. Behaviour of FRP-to-steel bonded joints, in: Chen, J.F., Teng, J.G. (Eds.), International Symposium on Bond Behaviour of FRP in Structures. International Institute for FRP in Construction, pp. 411–418.

Yang, J.Q., Smith, S.T., Feng, P., 2013. Effect of FRP-to-steel bonded joint configuration on interfacial stresses: Finite element investigation. Thin-Walled Structures 62, 215–228. https://doi.org/10.1016/j.tws.2012.07.020

Yu, Q.Q., Chen, T., Gu, X.L., Zhao, X.L., 2016. Boundary element analysis of edge cracked steel plates strengthened by CFRP laminates. Thin-Walled Structures 100, 147–157. https://doi.org/10.1016/j.tws.2015.12.016

Yu, Q.Q., Chen, T., Gu, X.L., Zhao, X.L., Xiao, Z.G., 2013. Fatigue behaviour of CFRP strengthened steel plates with different degrees of damage. Thin-Walled Structures 69, 10–17. https://doi.org/10.1016/j.tws.2013.03.012

Yu, Q.Q., Wu, Y.F., 2017. Fatigue strengthening of cracked steel beams with different configurations and materials. Journal of Composites for Construction 21, 04016093. https://doi.org/10.1061/(asce)cc.1943-5614.0000750

Yu, T., Fernando, D., Teng, J.G., Zhao, X.L., 2012. Experimental study on CFRP-to-steel bonded interfaces. Composites Part B: Engineering 43, 2279–2289. https://doi.org/10.1016/j.compositesb.2012.01.024

Yue, Q., Zheng, Y., Chen, X., Liu, X., 2016. Research on fatigue performance of CFRP reinforced steel crane girder. Composite Structures 154, 277–285. https://doi.org/10.1016/j.compstruct.2016.07.066

Zheng, B., Dawood, M., 2016. Debonding of carbon fiber–reinforced polymer patches from cracked steel elements under fatigue loading. Journal of Composites for Construction 20, 04016038. https://doi.org/10.1061/(ASCE)CC.1943-5614.0000694

Zheng, B., Dawood, M., 2016. Fatigue strengthening of metallic structures with a thermally-activated shape memory alloy (SMA) fiber-reinforced polymer (FRP) patch. Journal of Composites for Construction 1–11. https://doi.org/10.1061/(ASCE)CC.1943-5614.0000776.

Zheng, B.T., El-Tahan, M., Dawood, M., 2018. Shape memory alloy-carbon fiber reinforced polymer system for strengthening fatigue-sensitive metallic structures. Engineering Structures 171, 190–201. https://doi.org/10.1016/j.engstruct.2018.05.046

Appendix A Notation

a	Crack tip-to-mouth length
b	Width of a strip element
d	Dimension of the interfacial debonding zone
E_s	Elastic modulus of substrate
E_o	Elastic modulus of overlay
f, g	Geometric functions
G	Interfacial fracture energy
k	Interfacial stiffness
K	Stress intensity factor
L	Bond length
m	Weight function
N	Number of strip elements within the cracked segment
t_a	Thickness of adhesive layer
t_s	Half thickness of substrate plate
t_o	Thickness of overlay
u	Crack opening displacement
w	Half width of substrate plate
δ	Local interfacial slip
Δ	Global end-slip
δ_1	Elastic slip
δ_2	Plastic slip ($\delta_2 = \delta_1$ for a bi-linear bond-slip model)
δ_f	Debonding slip
ρ	Overlay-to-substrate stiffness ratio
σ	Far-end stress

σ_c	Correction overlay stress
σ_e	Effective crack-opening stress
σ_o	Overlay stress
σ_{pre}	overlay pre-stress
σ_s	Crack-opening stress (also known as the perturbation stress)
τ	Interfacial shear stress
τ_{max}	Maximum interfacial shear stress

Appendix B The global interfacial behavior model

The relationship between the global end-slip, Δ, and the force transferred via the interface, P, was given by (Fernando et al., 2014), and is adapted to the notation in the present paper as follows:

$$\begin{cases} P_1 = \dfrac{\tau_{max}\tanh\left(\lambda_1\dfrac{L}{2}\right)}{\lambda_1\delta_1}\Delta, \Delta < \delta_1 \\ P_2 = \tau_{max}c + \dfrac{\tau_{max}\tanh\left(\lambda_1\left(\dfrac{L}{2}-c\right)\right)}{\lambda_1\delta_1}\Delta, \delta_1 < \Delta < \delta_2 \\ P_3 = \dfrac{\tau_{max}\lambda_2}{\delta_1\lambda_1^2}\left(\dfrac{\lambda_1\delta_1}{\lambda_2}\left\{\tanh\left[\lambda_1\left(\dfrac{L}{2}-c_{max}-q\right)\right]+\lambda_1 c_{max}\right\}\cos(\lambda_2 q)+\left(\delta_f-\delta_2\right)\sin(\lambda_2 q)\right), \delta_2 < \Delta < \delta_f \\ P_4 = \dfrac{\tau_{max}\lambda_2\left(\delta_f-\delta_2\right)}{\delta_1\lambda_1^2\sin(\lambda_2 q_{max})}, \Delta > \delta_f \end{cases} \quad \text{(B1)}$$

where c and q are dimensions of the interfacial plastic and softening zones, respectively, and are related to Δ as follows:

$$\begin{cases} \Delta = \dfrac{\delta_1\lambda_1^2}{2}c^2 + \delta_1 + \lambda_1\delta_1 c\tanh\left(\lambda_1\left(\dfrac{L}{2}-c\right)\right), \delta_1 < \Delta < \delta_2 \\ c = c_{max} = \dfrac{1}{\lambda_1}\left[\sqrt{\left(2\dfrac{\delta_2}{\delta_1}-1\right)}-1\right], \Delta > \delta_2 \\ \Delta = \delta_f + \dfrac{\lambda_1\delta_1}{\lambda_2}\left\{\tanh\left[\lambda_1\left(\dfrac{L}{2}-c_{max}-q\right)\right]+\lambda_1 c_{max}\right\}\sin(\lambda_2 q) - \left(\delta_f-\delta_2\right)\cos(\lambda_2 q), \delta_2 < \Delta < \delta_f \\ q = q_{max} = \dfrac{1}{\lambda_2}\arctan\dfrac{\left(\delta_f-\delta_2\right)\lambda_2}{\lambda_1\delta_1(1+\lambda_1 c_{max})}, \Delta > \delta_f \end{cases} \quad \text{(B2)}$$

and λ_1 and λ_2 are coefficients defined by:

$$\begin{cases} \lambda_1 = \sqrt{\dfrac{\tau_{max}}{\delta_1\left(\dfrac{1}{E_s t_s}+\dfrac{1}{E_o t_o}\right)}} \\ \lambda_2 = \sqrt{\dfrac{\tau_{max}}{\left(\delta_f-\delta_2\right)\left(\dfrac{1}{E_s t_s}+\dfrac{1}{E_o t_o}\right)}} \end{cases} \quad \text{(B3)}$$

When Δ is larger than δ_f, the dimension of the debonding zone along the y axis, d, is calculated as follows:

$$d = \frac{\Delta-\delta_f}{P\left(\dfrac{1}{E_s t_s}+\dfrac{1}{E_o t_o}\right)}, \Delta > \delta_f \quad \text{(B4)}$$

The corresponding interfacial shear stress distribution, $\tau(y)$, adapted to the current notation, is as follows:

when $\Delta < \delta_1$,

$$\tau(y) = \frac{P_1 \lambda_1 \, cosh\big(\lambda_1 (L - y)\big)}{b \, sinh(\lambda_1 L)}, 0 \le y \le L \tag{B5}$$

when $\delta_1 \le \Delta < \delta_2$,

$$\begin{cases} \tau(y) = \tau_{max} \\ \tau(y) = \tau_{max} \dfrac{cosh\big(\lambda_1 (L - y)\big)}{cosh(\lambda_1 (L - c))} \end{cases} \tag{B6}$$

when $\delta_2 \le \Delta < \delta_f$,

$$\begin{cases} \tau(y) = \dfrac{\tau_{max}}{\delta_f - \delta_2} \left(\begin{array}{c} \dfrac{\lambda_1 \delta_1}{\lambda_2} \big(\tanh\big(\lambda_1 (L - c_{max} - q)\big) + \lambda_1 c_{max}\big) \sin\big(\lambda_2 (y - q)\big) \\ + \big(\delta_f - \delta_2\big) \cos\big(\lambda_2 (y - q)\big) \end{array} \right), 0 \le y \le q \\ \tau(y) = \tau_{max}, q \le y \le q + c_{max} \\ \tau(y) = \tau_{max} \dfrac{\cosh\big(\lambda_1 (L - y)\big)}{\cosh\big(\lambda_1 (L - c_{max} - q)\big)}, q + c_{max} \le y \le L \end{cases} \tag{B7}$$

and when $\Delta \ge \delta_f$,

$$\begin{cases} \tau(y) = \dfrac{\tau_{max}}{\delta_f - \delta_2} \left(\begin{array}{c} \dfrac{\lambda_1 \delta_1}{\lambda_2} \big(\tanh\big(\lambda_1 (L - d - c_{max} - q_{max})\big) + \lambda_1 c_{max}\big) \sin\big(\lambda_2 (y - q_{max} - d)\big) \\ + \big(\delta_f - \delta_2\big) \cos\big(\lambda_2 (y - q_{max} - d)\big) \end{array} \right), 0 \le y \le q \\ \tau(y) = \tau_{max}, \quad q_{max} + d \le y \le q_{max} + c_{max} + d \\ \tau(y) = \tau_{max} \dfrac{\cosh\big(\lambda_1 (L - y)\big)}{\cosh\big(\lambda_1 (L - c_{max} - q_{max} - d)\big)}, q_{max} + c_{max} + d \le y \le L \end{cases} \tag{B8}$$

Appendix C The overlay correction stress

The substrate plate displacement field in the strip element method is schematically shown in Figure C1a. At the end of the overlay, the strip-element substrate plate displacement, $\bar{D}_s(y = L)$, is non-uniform, whereas for a real center-cracked bare substrate plate subjected to the identical effective crack-opening stress, $\boldsymbol{\sigma_e}$, as shown in Figure C1b, the substrate plate displacement, $D_s|y = L$, is uniform. Therefore, there is a mismatch between $\bar{D}_s$ and D_s, and the former needs to be adjusted to the latter to obtain more accurate overlay stresses. The boundary condition for the overlay displacement is $\bar{D}_o(y = 0) = 0$, hence the displacement in the overlay can be related to the overlay stress as follows:

$$\bar{D}_o(y) = \frac{1}{E_o}\int_0^y \bar{\sigma}_o(y')dy' \tag{C1}$$

As the boundary condition for the axial stress distribution is $\bar{\sigma}_o(y = L) = 0$, the overlay stress can be related to the interfacial shear stress as:

$$\bar{\sigma}_o(y) = \frac{1}{t_o}\int_y^L \bar{\tau}(y')dy' \tag{C2}$$

where the shear stress distribution can be obtained from the crack opening displacement using Eqs. (B5)-(B8). Substituting (C2) into (C1) yields the following expression for the overlay displacement:

$$\bar{D}_o(y) = \frac{1}{E_o t_o}\int_0^y \int_{y'}^L \bar{\tau}(y'')dy''dy' \tag{C3}$$

For the strip element method, D_s is related to the displacement in the overlay, D_o, as:

$$\bar{D}_s(y) - \bar{D}_o(y) = \bar{\delta}(y) \tag{C4}$$

and in the perturbation state the interfacial slip is zero at the bondline-end, $\bar{\delta}(y = L) = 0$, which results in:

$$\overline{D}_s(y=L)=\overline{D}_o(y=L)=\frac{1}{E_o t_o}\int_0^L\int_{y'}^L \bar{\tau}(y'')dy''dy' \tag{C5}$$

The displacement field of the bare center-cracked substrate plate with a uniform stress applied on the crack face is given by (Tada et al., 2000) as follows:

$$\begin{cases} D(\alpha)=\dfrac{4\sigma w}{\pi E_s}\left(1-\dfrac{(1+\upsilon)}{2}\alpha\dfrac{\partial}{\partial\alpha}\right)\left(cosh^{-1}\left(\dfrac{cosh(\pi\alpha/2)}{cos(\pi a/(2w))}\right)-\pi\alpha/2\right), x=0 \\ D(\alpha)=\dfrac{4\sigma w}{\pi E_s}\left(1-\dfrac{(1+\upsilon)}{2}\alpha\dfrac{\partial}{\partial\alpha}\right)\left(cosh^{-1}\left(\dfrac{cosh(\pi\alpha/2)}{cos(\pi a/(2w))}\right)-\pi\alpha/2\right), x=w \end{cases} \tag{C6}$$

where $\alpha = y/w$. When α exceeds 2.5, the displacement across $0 \le x \le w$ converges to the following:

$$D_{s,\infty}=\frac{4\sigma_e w}{\pi E_s}ln\left(sec\left(\frac{\pi a}{2w}\right)\right) \tag{C7}$$

where σ_e is the uniform stress applied on the crack face. In the current model, the effective stress, which induces the crack opening, is non-uniform. As a simplification, σ_e is approximated as the value of σ_e at the crack mouth location, as the stress applied at the crack mouth has the maximum influence on the CODP, $\sigma_e = \sigma_e^{i=1}$. As a result, based on the assumption that the bond length is long enough, the real displacement in the substrate plate at $y = L$ is obtained as:

$$D_{s,\infty}=\frac{4\sigma_e^{i=1} w}{\pi E_s}ln\left(sec\left(\frac{\pi a}{2w}\right)\right) \tag{C8}$$

For the strip elements having $u_i > \delta_f$, $\overline{D}_s(y)$ is adjusted to $D_s(y)$ to mitigate the error induced by ignoring the interaction between neighboring strip-elements. This results in the correction interfacial shear stress, $\tau_c(y)$, due to this displacement adjustment. In the near-crack region, the substrate plate displacement field is dominated by the CODP and therefore no correction needs to be implemented, i.e., $\tau_c(y) = 0$ in the debonding, softening, and plastic zones. For the elastic zone, the shear stress needs to be corrected. Accordingly, the correction shear stress has the following expressions:

$$\begin{cases} \tau_c(y) = 0, 0 \le y \le c+q+d \\ \tau_c(y) = \tau_0 (y-c-q-d)^2 2^{-\lambda_1 (y-c-q-d)}, c+q+d < y \le L \end{cases} \tag{C9}$$

where τ_0 is the characteristic correction shear stress, and c, q, and d are the dimensions of the plastic, softening, and debonding zones, respectively. This correction of the shear stress in the elastic zone results in the correction of the overlay stress, σ_c, as follows:

$$\sigma_c = \frac{1}{t_o} \int_y^L \tau_c(y') dy' \tag{C10}$$

In turn, the overlay displacement expression becomes:

$$D_o(y) = \frac{1}{E_o t_o} \int_0^y \int_{y'}^L \left(\bar{\tau}(y'') - \tau_c(y'') \right) dy'' dy' \tag{C11}$$

and at $y = L$ it has the following boundary condition:

$$D_o(y = L) = D_{s,\infty} \tag{C12}$$

Substituting Eqs. (C8), (C9), and (C11) into Eq. (C12) yields the characteristic shear stress for the correction shear stress:

$$\tau_0 = \frac{E_o t_o \left(\bar{D}_s(y = L) - D_{s,\infty} \right)}{\left(\frac{6}{(ln(2)\,\lambda_1)^4} + \frac{2}{(ln(2)\,\lambda_1)^3} (c+q+d) \right)} \tag{C13}$$

Finally, the overlay correction stress at $y = 0$ is:

$$\sigma_c = \frac{E_o \left(\bar{D}_s(y = L) - D_{s,\infty} \right)}{\left(\frac{3}{(ln(2)\,\lambda_1)} + c + q + d \right)} \tag{C14}$$

Table 1. Values of parameters for CODP and SIF predictions

Case	ρ	a/w	σ [MPa]	L [mm]	Interfacial properties			
					Type	τ_{max}[MPa]	δ_1[mm]	δ_2[mm]	δ_f[mm]
1	*0.67*	*0.3*	*160~400*	*200*	Tri-linear (TL)	10	0.02	0.06	0.08
2	*0.33*	*0.5*							
3	*0.17*	*0.4*			Bi-linear (BL)	20	0.03	0.03	0.06
4	*0.10*	*0.2*							

Table 2. Values of parameters for near-crack debonding predictions

Case	a/w	ρ	σ [MPa]	L [mm]	Interfacial properties				
					Type	τ_{max}[MPa]	δ_1[mm]	δ_2[mm]	δ_f[mm]
1	0.4	0.067	240	200	Bi-linear (BL)	20	0.03	0.03	0.06
2			400						
3	0.5		240		Tri-linear (TL)	10	0.02	0.06	0.08
4			400						

Table 3. Values of parameters for near-crack debonding predictions

Study	Interfacial properties				ρ	FCG parameters	
	τ_{max}[MPa]	δ_1[mm]	δ_2[mm]	δ_f[mm]		C	m
Hu et al. (2021)	16.9	0.03	0.206	0.53	0.105	5.24×10^{-9}	1.46
Wang et al. (2015)					0.196	6.03×10^{-15}	3.639

Table 4. Values of parameters for the near-crack debonding examples

Case	ρ	a/w	σ [MPa]	L [mm]	Interfacial properties				
					Type	τ_{max}[MPa]	δ_1[mm]	δ_2[mm]	δ_f[mm]
1	0.112	0.4	150 250 350	200	Bi-linear (BL)	20	0.03	0.03	0.06
		0.2							
2		0.3	300						
		0.45							

Table 5. Values of parameters for SIF, near-crack debonding, and fatigue life predictions

Case	a/w	ρ	σ [MPa]	L [mm]	Interfacial properties				
					Name	τ_{max}[MPa]	δ_1[mm]	δ_2[mm]	δ_f[mm]
1	0.05, 0.1	0.223	300	200	IF-A	15	0.03	0.03	0.06

2	0.2, 0.3	IF-B	20	0.04	0.04	0.08
3	0.4, 0.5	IF-C	30	0.06	0.06	0.12
4		IF-D	15	0.1	0.9	1

Figure captions

Figure 1 Mechanical behavior of a metallic plate with a central crack: (a) schematic of a metallic crack; (b) dependence of SIF on applied load and crack length; (c) SIF range under fatigue loading; (d) crack growth rate versus SIF range in the log-log domain

Figure 2 Interfacial mechanical behavior: (a) bi-linear and tri-linear local bond-slip relationships; (b) four stages of interfacial shear stress distribution; (c) force transferred through the interface versus end-slip

Figure 3 Double-side FRP-overlaid plate with a central crack: (a) overview; (b) no-crack problem and near-end stress concentration; (b) perturbation problem and near-crack response

Figure 4 Discretization of cracked region ($0 \le x \le a$) into strip-elements: (a) in the x-y plane (b) 3D visualization of i^{th} strip-element

Figure 5 Flow chart of the iterative solution process for the implicit equation

Figure 6 Near-crack interfacial behavior, overlay stress, and crack opening in the perturbation problem

Figure 7 CODP predictions for bare plates from the analytical and the FE models: (a) 2D FE model of a bare plate with a central crack; (b) comparisons between analytical and FE predictions

Figure 8 CODP predictions for centrally-cracked plates bonded with overlays from the analytical and the FE models: (a) overview of FE model; (b) overlay mesh and boundary conditions; (c) comparison of CODP results

Figure 9 CODP and SIF predictions from the analytical and the FE models for different cases: (a) CODP results; (b) SIF results

Figure 10 Predictions of near-crack interfacial behavior: (a) − (b) contours of near-crack interfacial shear stress; (c) − (d) interfacial shear stress distributions along the centerline; (e) − (f) overlay stress distributions along the crack line

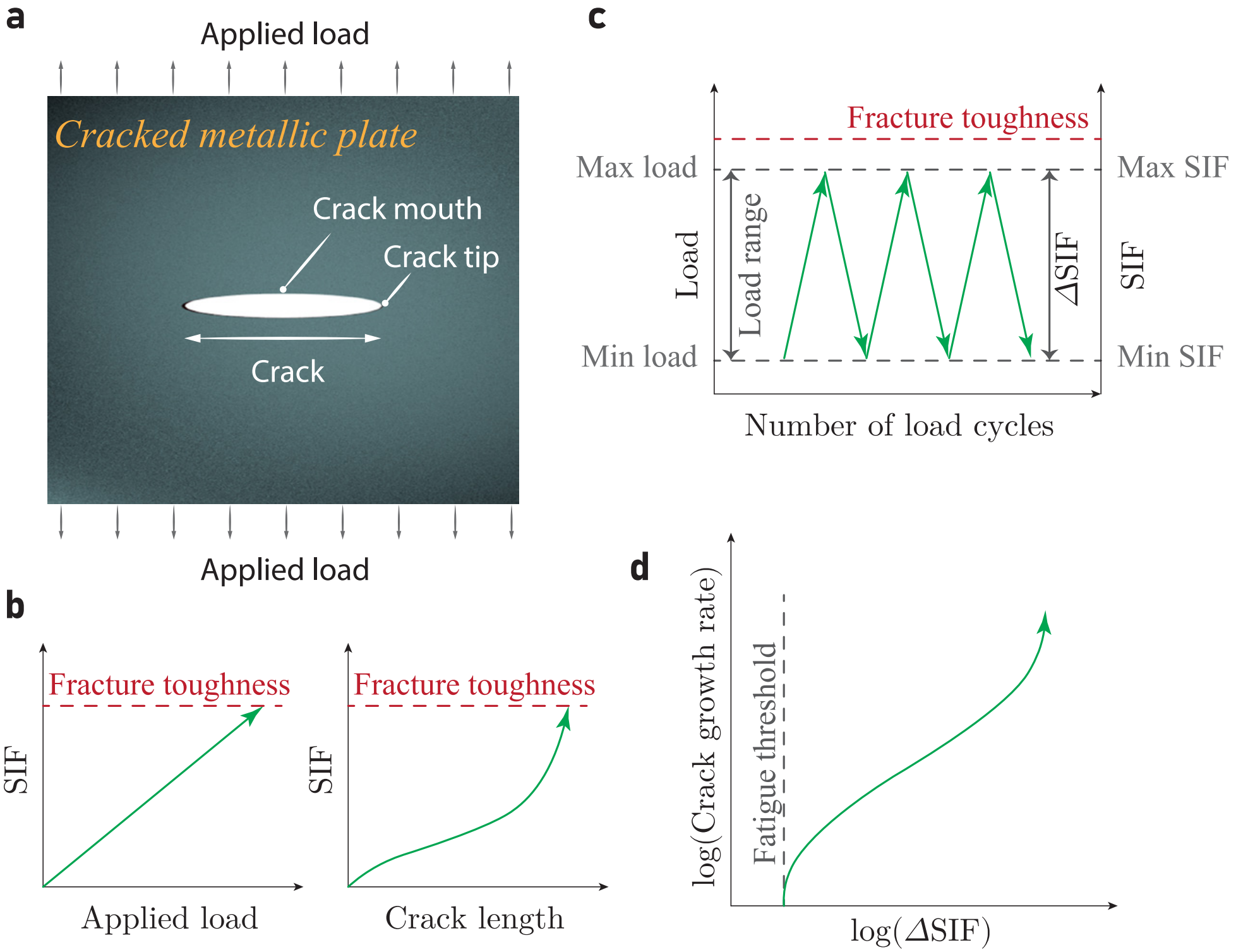
a
Applied load
Cracked metallic plate
Crack mouth
Crack tip
Crack
Applied load
b
Fracture toughness
SIF
Applied load
Fracture toughness
SIF
Crack length
c
Fracture toughness
Max load
Max SIF
Load
Load range
ΔSIF
SIF
Min load
Min SIF
Number of load cycles
d
log(Crack growth rate)
Fatigue threshold
log(ΔSIF)

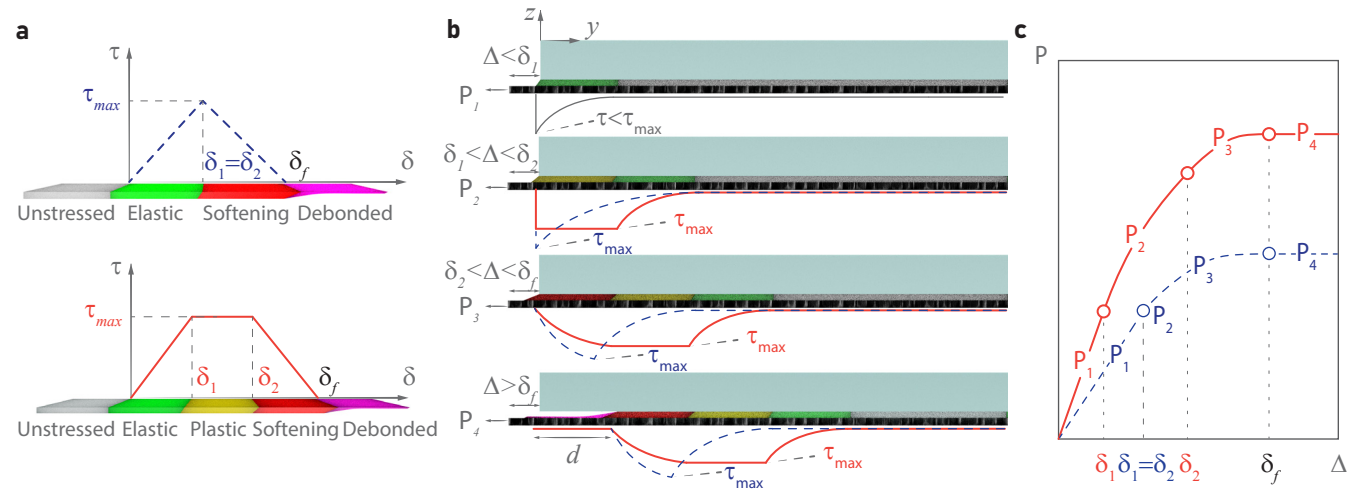
a
τ
τmax
δ1=δ2
δf
δ
Unstressed Elastic Softening Debonded
τ
τmax
δ1
δ2
δf
δ
Unstressed Elastic Plastic Softening Debonded
b
z
y
Δ<δ1
P1
τ<τmax
δ1<Δ<δ2
P2
τmax
τmax
δ2<Δ<δf
P3
τmax
τmax
Δ>δf
P4
d
τmax
τmax
c
P
P1
P2
P3
P4
P3
P4
P2
P1
δ1 δ1=δ2 δ2
δf
Δ

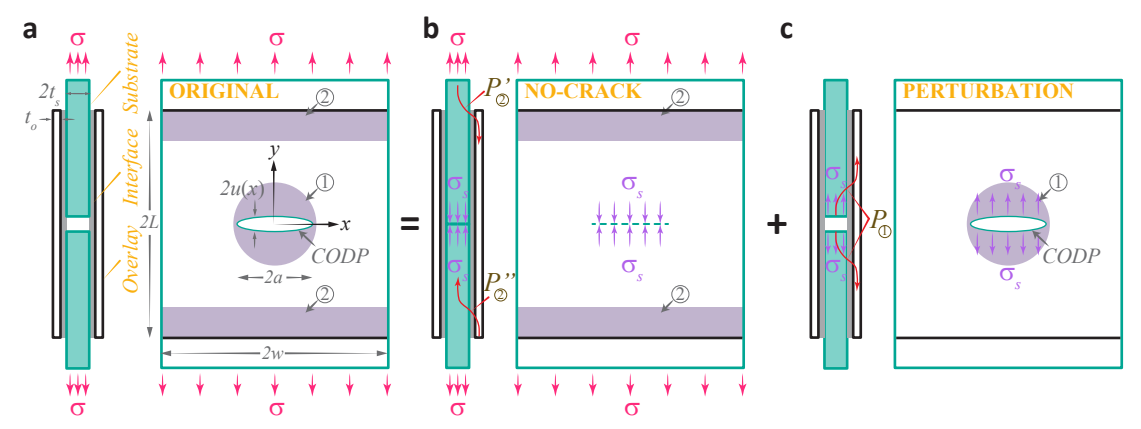
a
b
c
σ
2t_s
t_o
Substrate
Interface
Overlay
ORIGINAL
2L
y
x
2u(x)
①
②
CODP
2a
2w
=
P'②
P''②
NO-CRACK
σ_s
+
P①
PERTURBATION

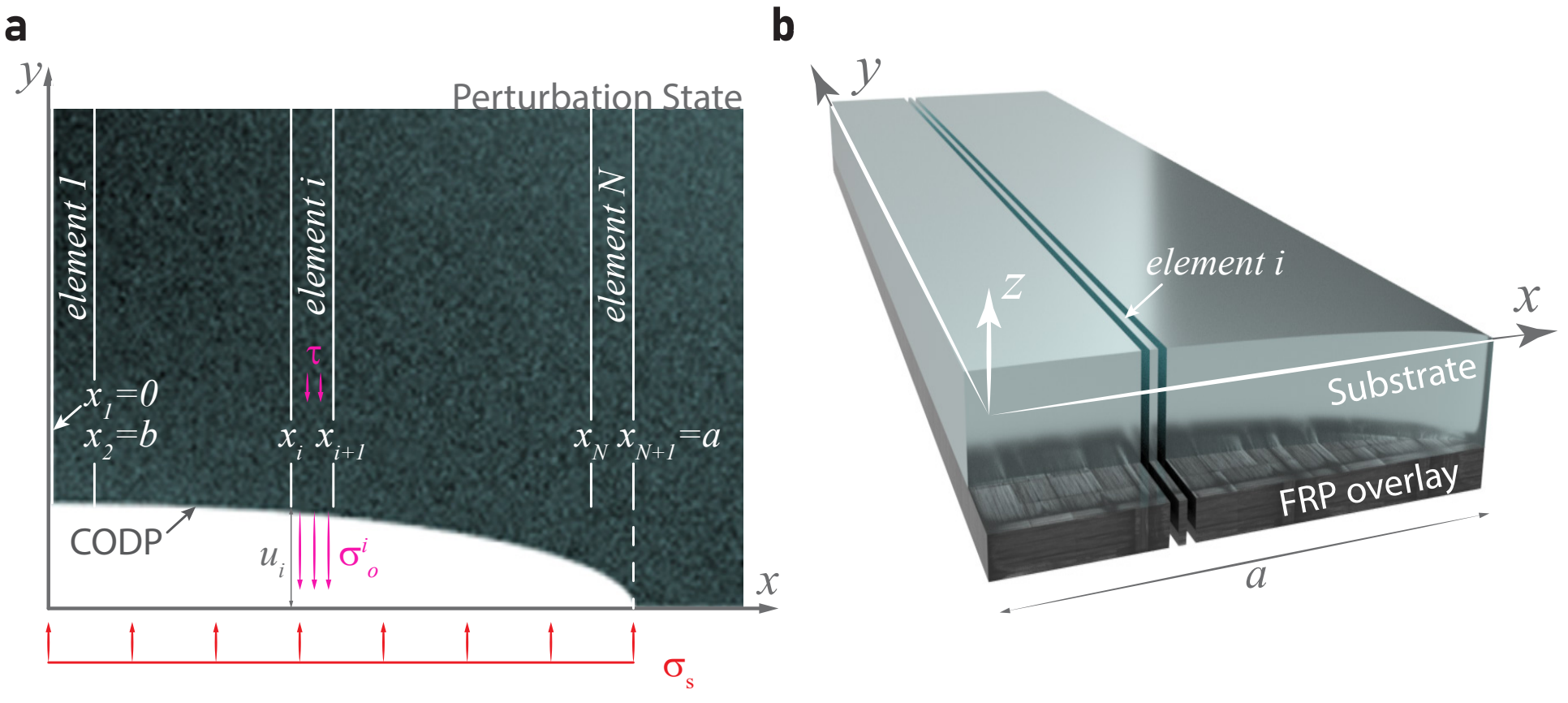
a
y
Perturbation State
element 1
element i
element N
τ
$x_1=0$
$x_2=b$
x_i x_{i+1}
x_N $x_{N+1}=a$
CODP
u_i
σ^i_o
x
σ_s
b
y
z
element i
x
Substrate
FRP overlay
a

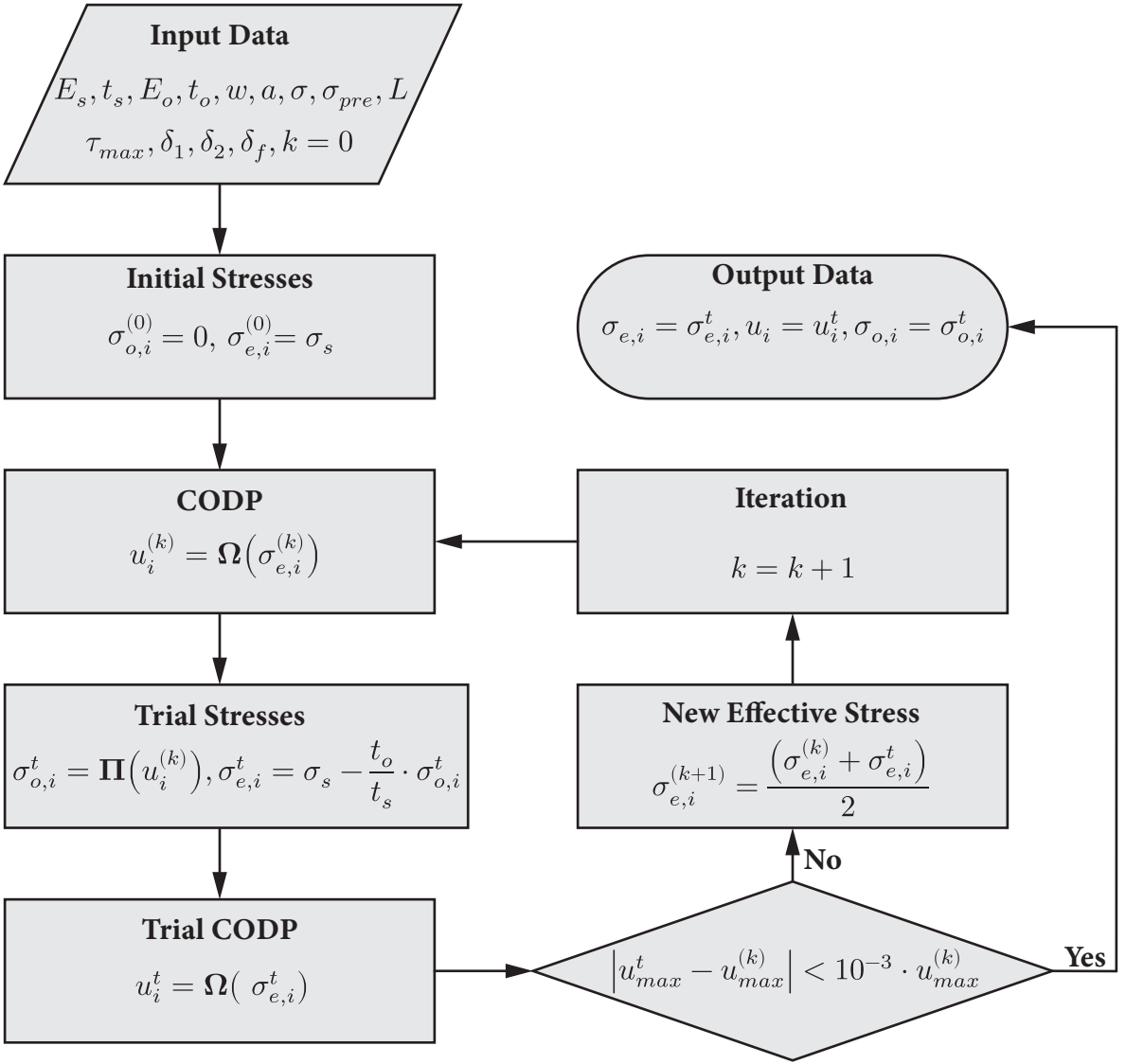
Input Data
$E_s, t_s, E_o, t_o, w, a, \sigma, \sigma_{pre}, L$
$\tau_{max}, \delta_1, \delta_2, \delta_f, k = 0$
Initial Stresses
$\sigma_{o,i}^{(0)} = 0,\ \sigma_{e,i}^{(0)} = \sigma_s$
CODP
$u_i^{(k)} = \mathbf{\Omega}\left(\sigma_{e,i}^{(k)}\right)$
Trial Stresses
$\sigma_{o,i}^{t} = \mathbf{\Pi}\left(u_i^{(k)}\right), \sigma_{e,i}^{t} = \sigma_s - \frac{t_o}{t_s} \cdot \sigma_{o,i}^{t}$
Trial CODP
$u_i^t = \mathbf{\Omega}(\ \sigma_{e,i}^t)$
$\left|u_{max}^t - u_{max}^{(k)}\right| < 10^{-3} \cdot u_{max}^{(k)}$
No
Yes
New Effective Stress
$\sigma_{e,i}^{(k+1)} = \frac{\left(\sigma_{e,i}^{(k)} + \sigma_{e,i}^{t}\right)}{2}$
Iteration
$k = k + 1$
Output Data
$\sigma_{e,i} = \sigma_{e,i}^t, u_i = u_i^t, \sigma_{o,i} = \sigma_{o,i}^t$

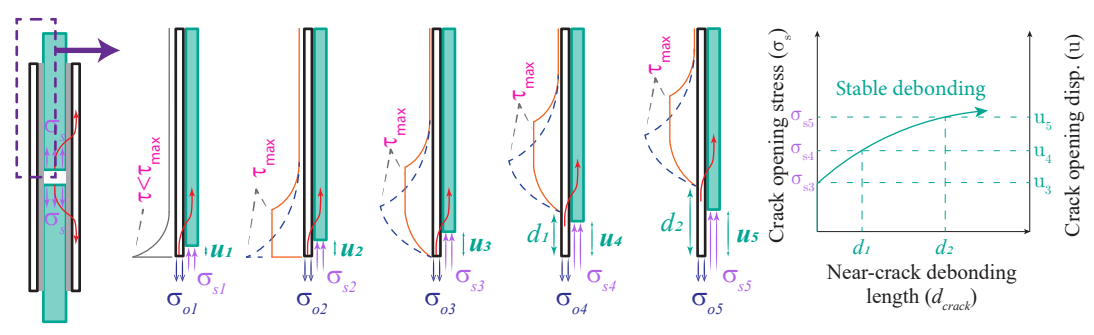
$\tau<\tau_{max}$
τ_{max}
u_1
u_2
u_3
u_4
u_5
d_1
d_2
σ_{s1}
σ_{s2}
σ_{s3}
σ_{s4}
σ_{s5}
σ_{o1}
σ_{o2}
σ_{o3}
σ_{o4}
σ_{o5}
Crack opening stress (σ_s)
Crack opening disp. (u)
Stable debonding
Near-crack debonding length (d_{crack})

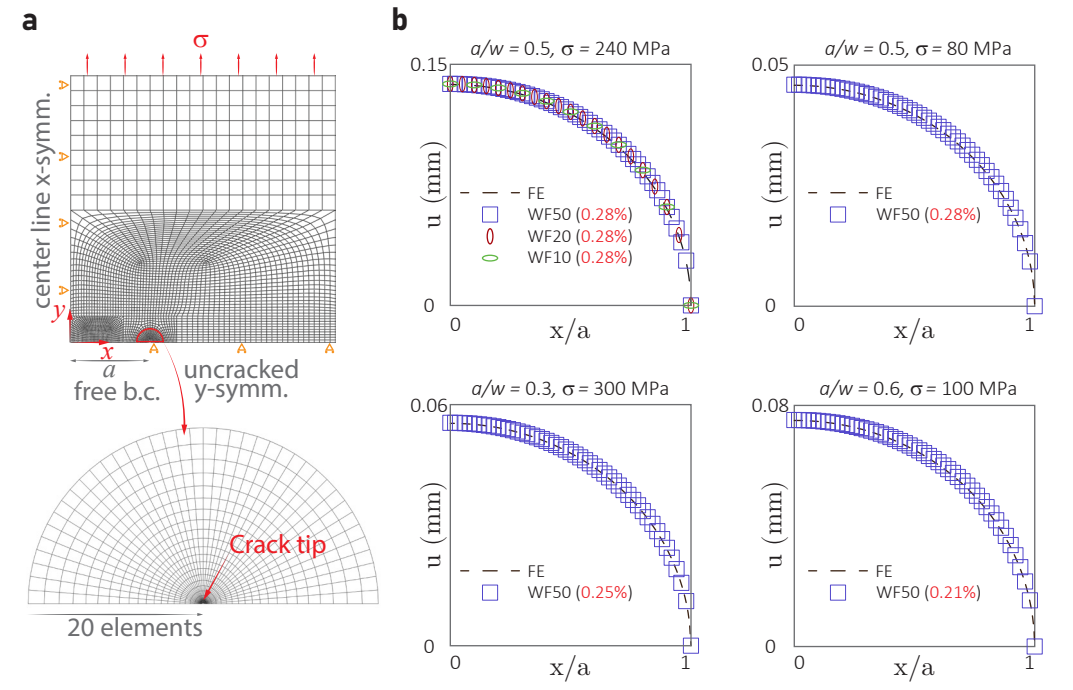
a
σ
center line x-symm.
A
y
x
a
free b.c.
uncracked
y-symm.
Crack tip
20 elements
b
a/w = 0.5, σ = 240 MPa
0.15
0
u (mm)
x/a
1
FE
WF50 (0.28%)
WF20 (0.28%)
WF10 (0.28%)
a/w = 0.5, σ = 80 MPa
0.05
WF50 (0.28%)
a/w = 0.3, σ = 300 MPa
0.06
WF50 (0.25%)
a/w = 0.6, σ = 100 MPa
0.08
WF50 (0.21%)

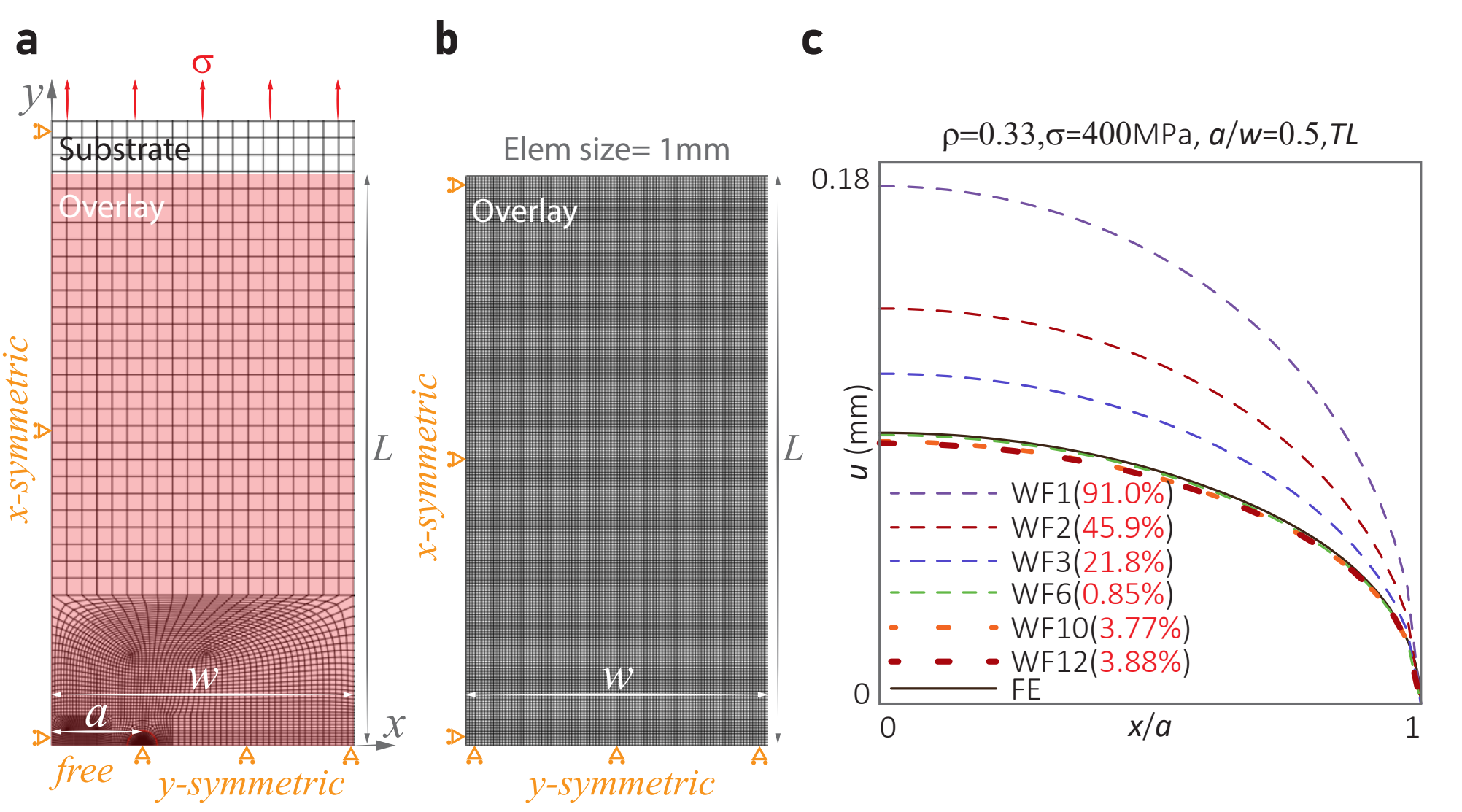
a
σ
y
Substrate
Overlay
x-symmetric
L
w
a
x
free
y-symmetric
b
Elem size= 1mm
Overlay
x-symmetric
L
w
y-symmetric
c
ρ=0.33,σ=400MPa, a/w=0.5,TL
0.18
0
u (mm)
WF1(91.0%)
WF2(45.9%)
WF3(21.8%)
WF6(0.85%)
WF10(3.77%)
WF12(3.88%)
FE
0
x/a
1

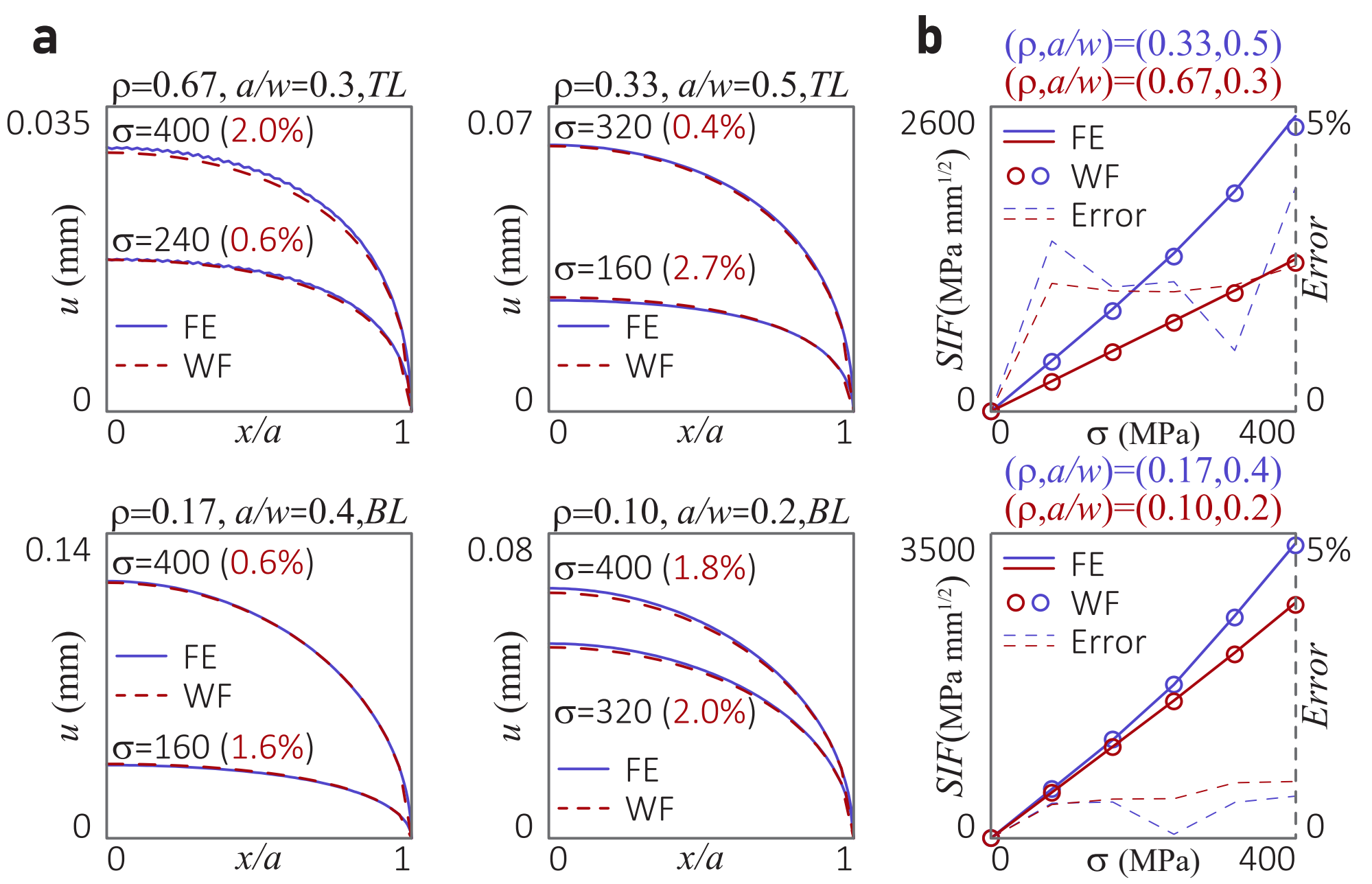
a
ρ=0.67, a/w=0.3,TL
0.035
σ=400 (2.0%)
σ=240 (0.6%)
u (mm)
FE
WF
0
0
x/a
1
ρ=0.33, a/w=0.5,TL
0.07
σ=320 (0.4%)
σ=160 (2.7%)
u (mm)
FE
WF
0
0
x/a
1
ρ=0.17, a/w=0.4,BL
0.14
σ=400 (0.6%)
FE
WF
σ=160 (1.6%)
u (mm)
0
0
x/a
1
ρ=0.10, a/w=0.2,BL
0.08
σ=400 (1.8%)
σ=320 (2.0%)
u (mm)
FE
WF
0
0
x/a
1
b
(ρ,a/w)=(0.33,0.5)
(ρ,a/w)=(0.67,0.3)
2600
5%
FE
WF
Error
SIF(MPa mm1/2)
Error
0
0
σ (MPa)
400
(ρ,a/w)=(0.17,0.4)
(ρ,a/w)=(0.10,0.2)
3500
5%
FE
WF
Error
SIF(MPa mm1/2)
Error
0
0
σ (MPa)
400

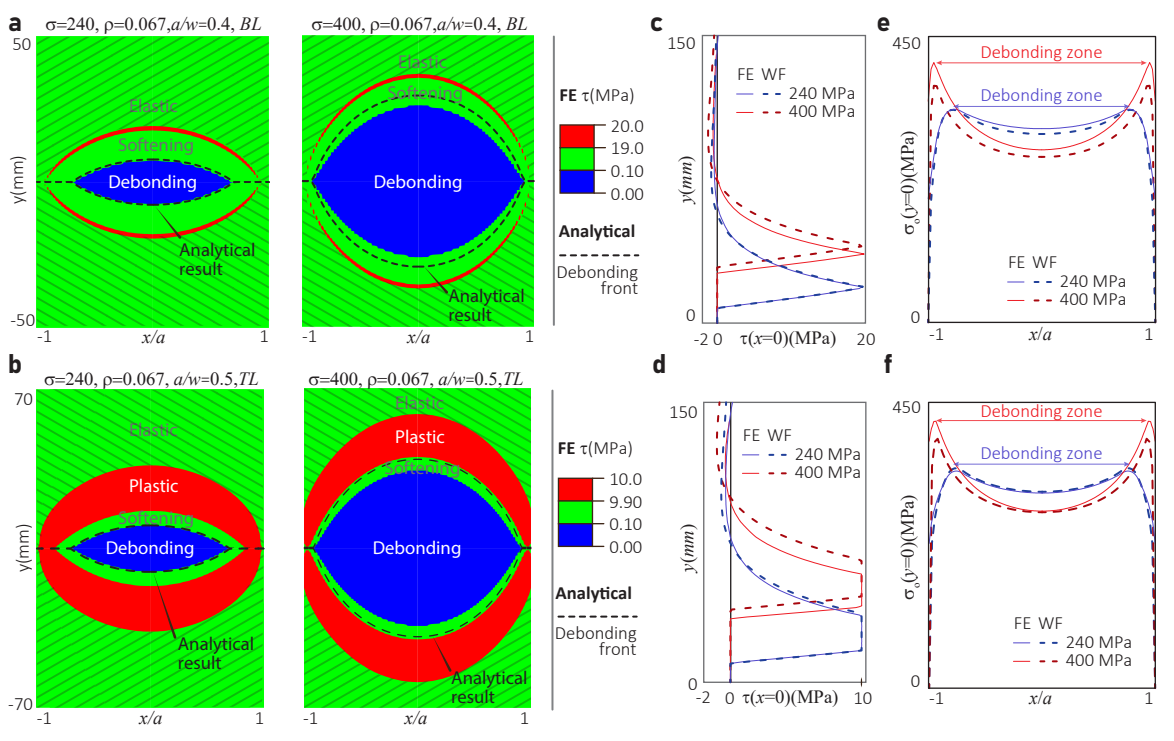
a
σ=240, ρ=0.067,a/w=0.4, BL
σ=400, ρ=0.067,a/w=0.4, BL
Elastic
Softening
Debonding
Analytical result
y(mm)
x/a
b
σ=240, ρ=0.067, a/w=0.5,TL
σ=400, ρ=0.067, a/w=0.5,TL
Plastic
FE τ(MPa)
20.0
19.0
0.10
0.00
10.0
9.90
Analytical
Debonding front
c
d
FE WF
240 MPa
400 MPa
τ(x=0)(MPa)
e
f
Debonding zone
σ0(y=0)(MPa)

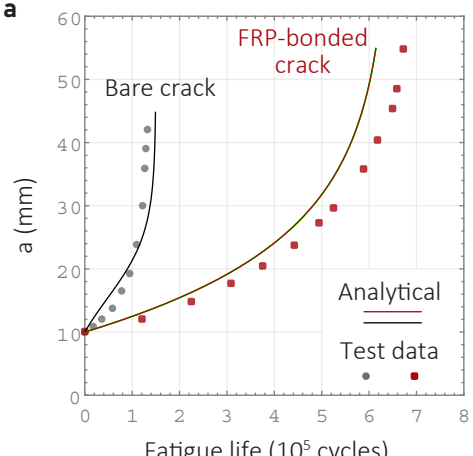
a
a (mm)
Fatigue life (10^5 cycles)
Bare crack
FRP-bonded crack
Analytical
Test data
b
a (mm)
Fatigue life (10^5 cycles)
Bare crack
FRP-bonded crack
Analytical
Test data

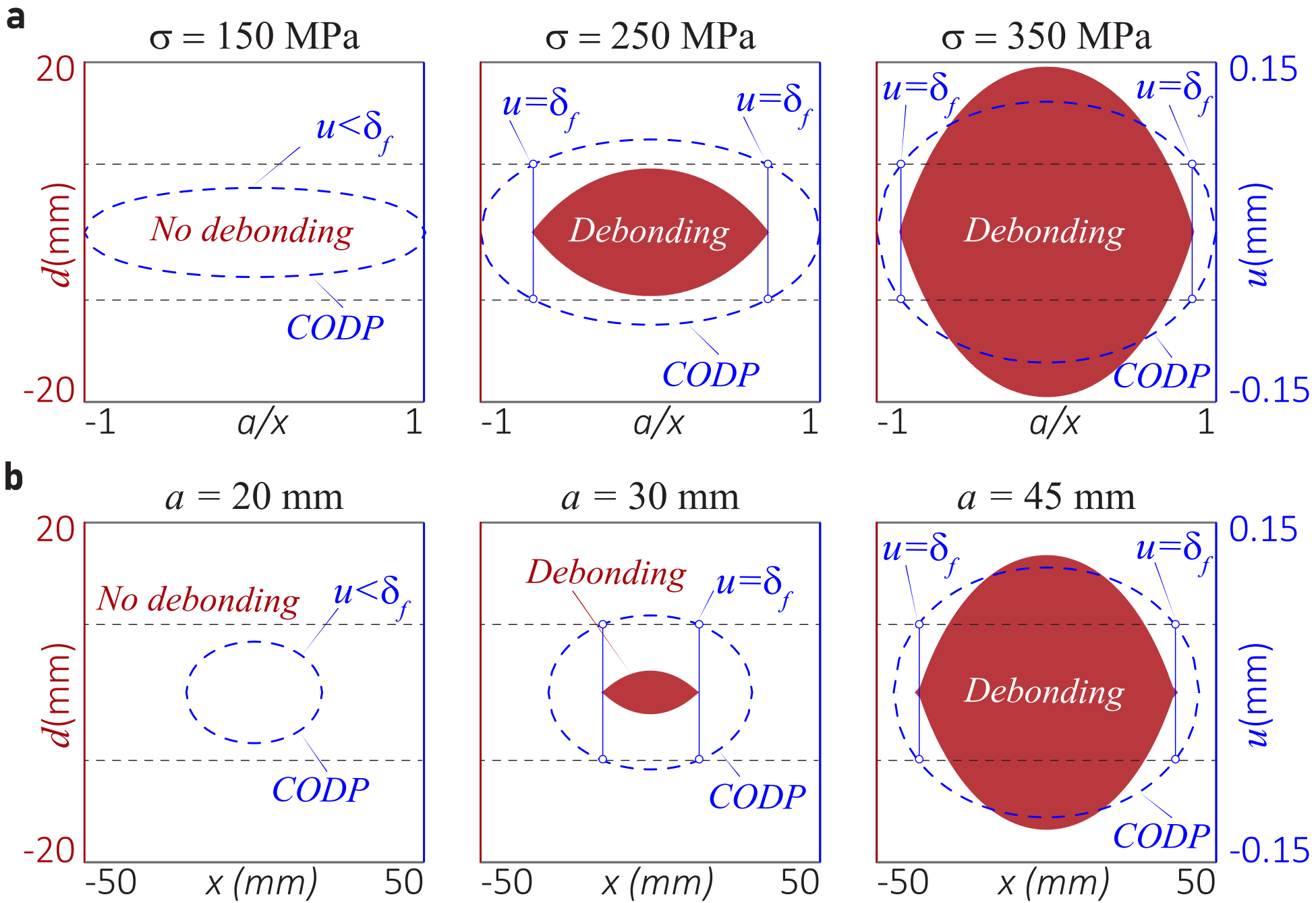
a
σ = 150 MPa
σ = 250 MPa
σ = 350 MPa
20
-20
d(mm)
u<δf
No debonding
CODP
u=δf
Debonding
CODP
0.15
-0.15
u(mm)
-1
a/x
1
b
a = 20 mm
a = 30 mm
a = 45 mm
x (mm)
-50
50

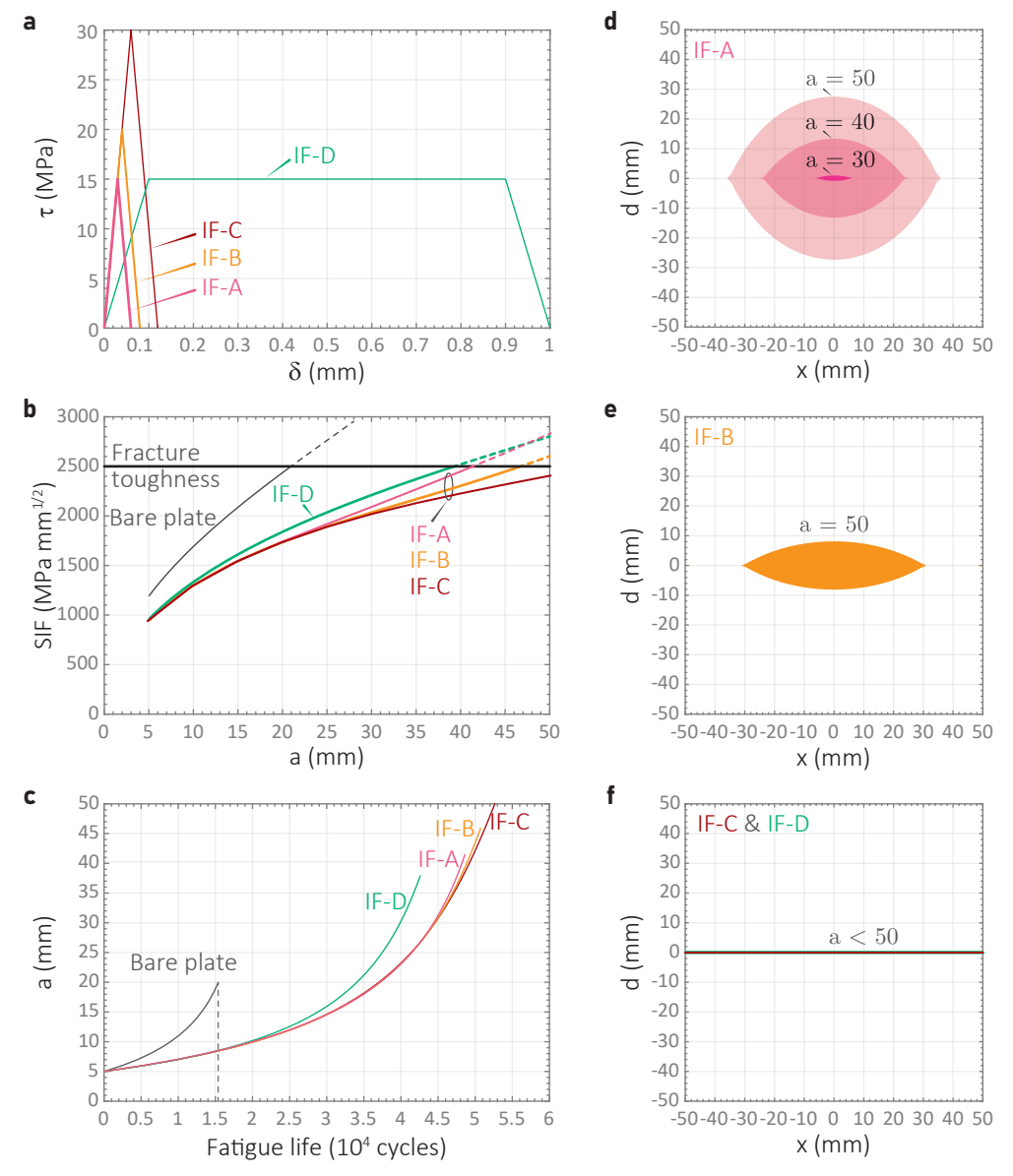
a
τ (MPa)
δ (mm)
IF-D
IF-C
IF-B
IF-A
b
SIF (MPa mm^1/2)
a (mm)
Fracture toughness
Bare plate
IF-D
IF-A
IF-B
IF-C
c
a (mm)
Fatigue life (10^4 cycles)
Bare plate
IF-D
IF-A
IF-B
IF-C
d
IF-A
a = 50
a = 40
a = 30
d (mm)
x (mm)
e
IF-B
a = 50
d (mm)
x (mm)
f
IF-C & IF-D
a < 50
d (mm)
x (mm)